

# We are IntechOpen, the world's leading publisher of Open Access books Built by scientists, for scientists

4,800

Open access books available

122,000

International authors and editors

135M

Downloads

Our authors are among the

154

Countries delivered to

TOP 1%

most cited scientists

12.2%

Contributors from top 500 universities



WEB OF SCIENCE™

Selection of our books indexed in the Book Citation Index  
in Web of Science™ Core Collection (BKCI)

Interested in publishing with us?  
Contact [book.department@intechopen.com](mailto:book.department@intechopen.com)

Numbers displayed above are based on latest data collected.  
For more information visit [www.intechopen.com](http://www.intechopen.com)



---

# Subwavelength and Nanometer Diameter Optical Polymer Fibers as Building Blocks for Miniaturized Photonics Integration

---

Xiaobo Xing, Huaqing Yu, Debin Zhu, Jiapeng Zheng, Huang Chen, Wei Chen and Jiye Cai

Additional information is available at the end of the chapter

<http://dx.doi.org/10.5772/47822>

---

## 1. Introduction

The development of nanotechnology in photonics offers significant scientific and technological potentials for miniaturized photonic integrated circuits (PICs) [1,2]. It fosters the substantial efforts for exploring novel materials, developing easy fabrication techniques, reducing the size of photonic components, improving device integration density, and fabricating low-cost nanodevices. One-dimensional (1D) nanomaterials are promising candidates for photonics integration due to their intriguing optical, electronic, and mechanical properties [3-9]. In 2003, L. Tong et al. experimentally demonstrated low-loss optical waveguiding in silica micro/nanofibers (MNFs) with diameters far below the wavelength of the guided light [10], which renewed research interests in optical MNFs as potential building blocks for applications in high density and miniaturized PICs [11-22]. In particular, polymers have been widely regarded as useful materials for manipulating light in optical waveguide applications due to their good processability, biocompatibility, tunable properties, flexibility, and low cost for integration [15-22]. On the other hand, polymeric materials offer a unique opportunity to carry other chemical composition and to readily produce hybrid nanocomposites. 1D nanostructures fabricated from polymers have been the hot subject of recent research with regard to their special physical, chemical, electronic, and photonic properties [19,23-38]. Demonstration of viable polymer MNF based elements and architectures will require the development of reliable methods for the production of such structures with good control over critical parameters such as diameter, length, morphology, and chemical composition. Up to now, a bunch of new materials and new techniques have been developed to fabricate subwavelength and nanometer diameter polymer fibers, including electrospinning, phase separation, self assembling and one-step drawing, etc. [29].

Polymer MNFs with diameter down to several nanometers and length up to hundreds of millimeters have been reported. Besides its low cost and tiny size, polymer MNFs are easy to couple with other general optical devices, enabling them to fulfill their potentials in optical functions. Due to their good flexibility and large tunability, many shapes and structures can be achieved from polymer MNFs, including optical splitters [18,30], resonator [31], couplers [32], Mach–Zehnder Interferometers (MZI) [33], light-emitting polymer nanofibers [34], photodetector [35], organic nanofiber laser [36], sensors [37,38], polymeric nanofiber architecture [38].

In this chapter, we will introduce the fabrication techniques of polymer MNFs. Then we will focus on polymer MNF-based elements and assess their potential used as passive and active components in miniaturized photonic devices. Finally is a perspective.

## **2. Fabrication methods of polymer MNFs**

A number of different techniques including physical, chemical, thermal, and electrostatic method have been used to fabricate polymer MNFs. Ten of these fabrication methods are briefly described in the following section [29].

### **2.1. Electrospinning**

Electrospinning is an electrostatically driven method of fabricating polymer nanofibers. Nanofibers are formed from a liquid polymer solution or melt that is fed through a capillary tube into a region of high electric field [39]. The electric field is most commonly generated by connecting a high voltage power source in the kilovolt range to the capillary tip (Fig. 1). As electrostatic forces overcome the surface tension of the liquid, a Taylor cone is formed and a thin jet is rapidly accelerated to a grounded or oppositely charged collecting target. Instabilities in this jet cause violent whipping motions that elongate and thin the jet allowing the evaporation of some of the solvent or cooling of melts to form solid nanofibers on the target site. Nanofiber size and microstructure can be controlled by several processing parameters including: solution viscosity, voltage, feed rate, solution conductivity, capillary to collector distance, and orifice size [40]. The electrospinning technique is very versatile and a wide range of polymer and copolymer materials with a wide range of fiber diameters (several nanometers to several microns) can be fabricated using this technique. Many different types of molecules can be easily incorporated during the electrospinning fabrication process to produce functionalized nanofibers. Electrospun nanofibers are usually collected from an electrospinning jet as non-woven randomly or uniaxially aligned sheets or arrays.

### **2.2. Phase separation**

Nanofibrous foam materials have been fabricated by a technique called thermally induced liquid-liquid phase separation [41]. This fabrication procedure involves (a) the dissolution of polymer in solvent (b) phase separation and polymer gelatination in low temperature (c)

solvent exchange by immersion in water and (d) freezing and freeze-drying (Fig. 2). The morphology of these structures can be controlled by fabrication parameters such as gelatination temperature and polymer concentration. Interconnected porous nanofiber networks have been formed from polymers such as, poly-L-lactide acid (PLLA), poly-lactic-co-glycolic acid (PLGA), and poly-DL-lactic acid (PDLA) with fiber diameters from 50–500 nm, and porosities up to 98.5%.

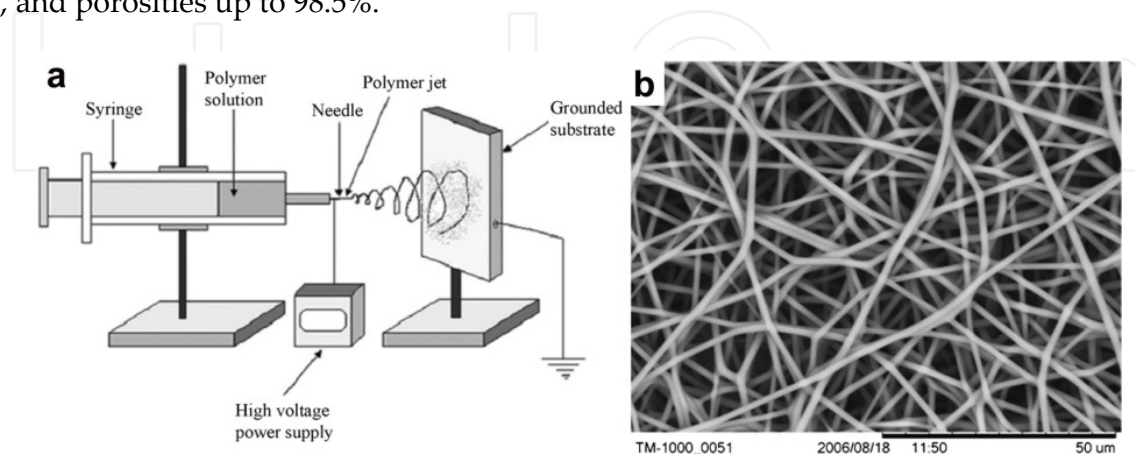


**Figure 1.** (a) schematic of a standard electrospinning setup [39] and a scanning electron microscope (SEM) image (b) of electrospun polyurethane nanofibers.

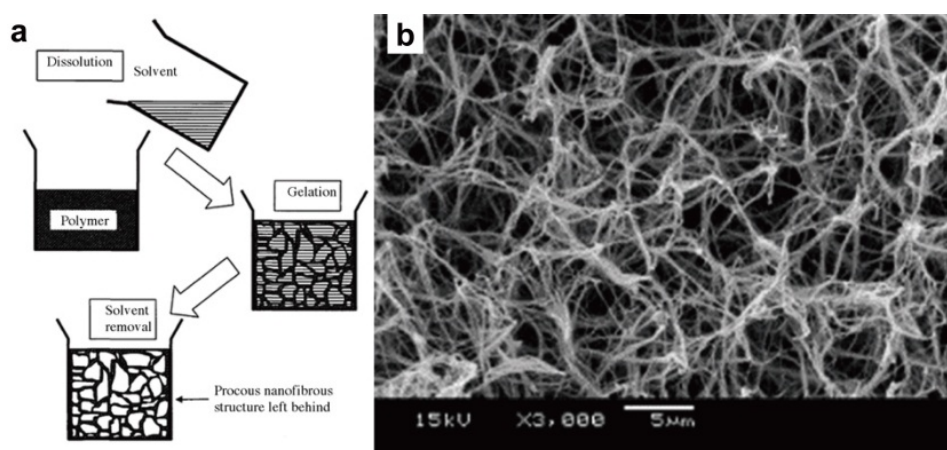


**Figure 2.** A schematic (a) of nanofiber formation by phase separation [42], and an SEM image (b) of nanofibrous structure fabricated by this technique [41].

### 2.3. Self assembly

Self assembly is a process by which molecules organize and arrange themselves into patterns or structures through non-covalent forces such as hydrogen bonding, hydrophobic forces, and electrostatic reactions. Dialkyl chain amphiphiles containing peptides were developed to mimic the ECM. These peptide amphiphiles (PA), derived from a collagen ligand, allow for a self assembling system that consists of a hydrophobic tail group and a hydrophilic head group [43]. Figure 3 shows the hierarchy of structure found in the self-assembled PA nanofiber networks [44]. The specific composition of amino acid chains in peptide amphiphile systems determines the assembly, chemical, and biological properties of

the system, and therefore PA systems can be tailored to specific applications [45,46]. Nanofibers with diameters around 5–25 nm can be formed by the self assembly process. Cells can be encapsulated in a nanofibrous PA structure if they are added during the self assembly process and PA can also be injected in vivo where they subsequently self assemble into a nanofibrous network. It has been demonstrated that self assembled peptide nanofibers can spontaneously undergo reassembly back to a nanofibers scaffold after destruction by sonication, and after multiple cycles of destruction and reassembly, the peptide nanofibers scaffolds were still indistinguishable from their original structures [47].

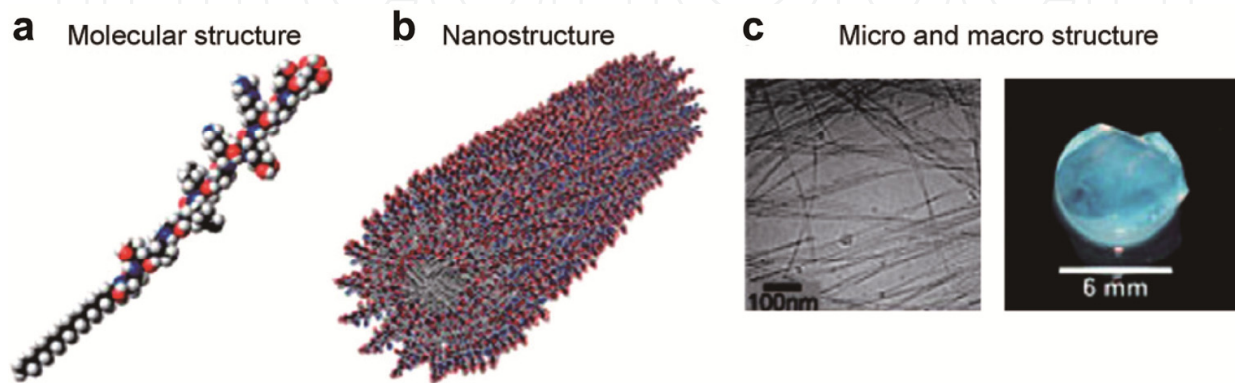


**Figure 3.** Schematics of the (a) molecular structure and (b) nanostructure, and images of the (c) micro and macro structure of a self assembling peptide amphiphile nanofiber network [44].

#### 2.4. One-step drawing technique

Nanofibers can be mechanically drawn from viscous polymer liquids directly [48]. In one example, nanofibers were drawn directly when a rod was placed in a polymer melt and moved up forming a thin filament that cooled to form a nanofiber [17]. Figure 4 shows the schematic illustration of the drawing process. Fig. 4a shows a vertical direction tip-drawing process. Poly(trimethylene terephthalate) (PTT) pellets (melt temperature  $T_m = 225^\circ\text{C}$ ) was melt by a heating plate and the temperature was kept at around  $250^\circ\text{C}$  during the wire drawing. First, an iron or silicarod/tip with radius of about  $125\ \mu\text{m}$  is being approached and its tip is immersed into the molten PTT. Then the rod tip is retracted from the molten PTT with a speed of 0.1–1 m/s, leaving a PTT wire extending between the molten PTT and the tip. The extended PTT wire is quickly quenched in air and finally, a naked amorphous PTT nanowire is formed. PTT nanofibers with diameters as low as 60 nm, and lengths up to 500 mm have been achieved. A SEM image (Fig. 4b) shows part of the coiled nanofiber with a length of about 200 mm and an average diameter of 280 nm. The diameter variation ratio is about  $8.4 \times 10^{-8}$ . Figure 4c demonstrates flexible and elastic connection by pulling the polymer nanofibers with diameters of 140 and 170 nm. To examine surface roughness of the polymer nanofibers, high-magnification transmission electron microscope (TEM) was done. Figure 4d shows a TEM image of a 190-nm-diameter nanowire, indicating no visible defect and irregularity on the surface of the polymer nanofiber. Typical average sidewall root-mean-square roughness of the polymer nanofiber is 0.28 nm. The electron diffraction pattern (inset of Fig. 4d) demonstrates that the obtained PTT MNF is amorphous. The results demonstrate



that the obtained polymer nanofibers exhibit high surface smoothness, length uniformity, high mechanical properties, and excellent flexibility.

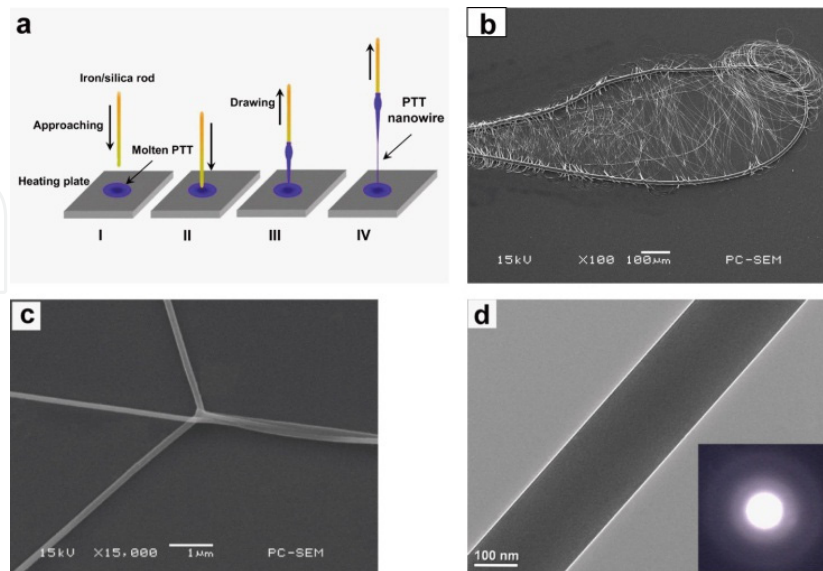


**Figure 4.** Schematic of nanofiber fabrication by the drawing technique. (b) SEM images of a nanofiber with average diameter of 280 nm coiled on a 12- $\mu\text{m}$ -diameter PTT bending rod, the length of the nanofiber displayed is about 200 mm. (c) Flexible and elastic enough nanofiber connection with diameters of 140 and 170 nm. (d) Transmission electron microscope (TEM) image of a 190-nm-diameter fiber. The inset shows its electron diffraction pattern [17,18].

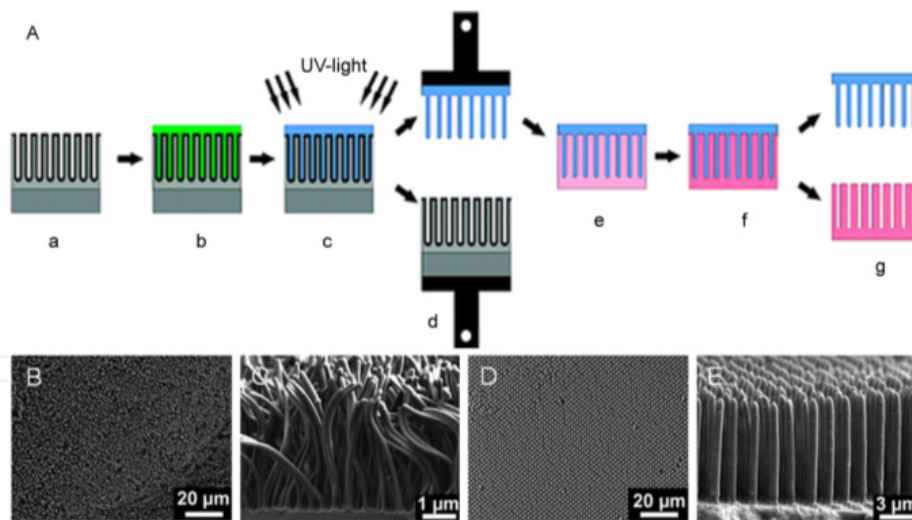


**Figure 5.** (A) Schematic of the fabrication of polymer nanofibers using a nondestructive templating technique (grey: alumina template, green: resin, blue: polymer nanofibers, pink: silica replica template). (B-E) SEM images of 120 nm (b&c) and 1 $\mu\text{m}$  (d&e) polymer fibers fabricated by the above technique [49].

## 2.5. Templating

Polymer nanofibers can be fabricated using templates such as self-ordered porous alumina. Alumina network templates with pore diameters from 25 to 400 nm, and pore depths from around 100 nm to several 100  $\mu\text{m}$  have been fabricated. Polymer nanofiber arrays can be

released from these molds by destruction of the molds or mechanical detachment (Fig. 5) [49,50]. The length of polycaprolactone (PCL) nanofibers fabricated from alumina templates can be controlled as a function of parameters such as melt time and temperature [51].

## 2.6. Vapor-phase polymerization

Polymer MNFs have also been fabricated from vapor-phase polymerization. Plasma-induced polymerization of vapor phase vinyltrichlorosilane produced organosiloxane fibers with diameters around 25 nm and typical lengths of 400–600 nm and cyanoacrylate fibers with diameters from 100 to 400 nm and lengths of hundreds of microns (Fig. 6) [52,53].

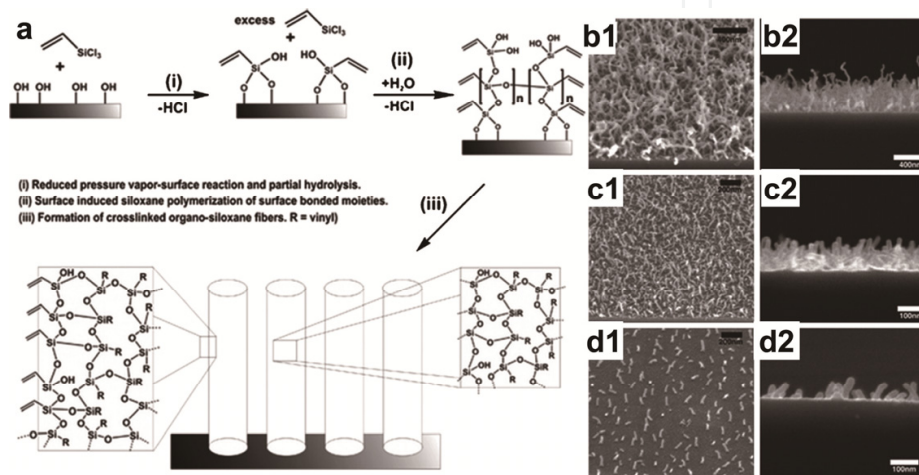


**Figure 6.** (a) Schematic describing a proposed mechanism for nanofiber formation by vapor-phase polymerization (b) Aerial (1) and side views (2) of polymer nanofibers fabricated from vapor-phase polymerization at high (b), intermediate (c) and low (d) packing densities [52].

## 2.7. Extraction

Nanofibers can be extracted from natural materials using chemical and mechanical treatments. Cellulose fibrils can be disintegrated from plant cell walls. In one example, cellulose nanofibers were extracted from wheat straw and soy hull with diameters ranging from 10 to 120 nm and lengths up to a few thousand nanometers (Fig. 7) [54]. Invertebrates have also been used as a source for the extraction of nanofibers. Chitin nanofibers 3–4 nm in diameter and a few micrometers in length were extracted from squid pen and Poly-N-acetyl glucosamine nanofibers isolated from a marine diatom demonstrated prothrombotic interactions with red blood cells [55,56].

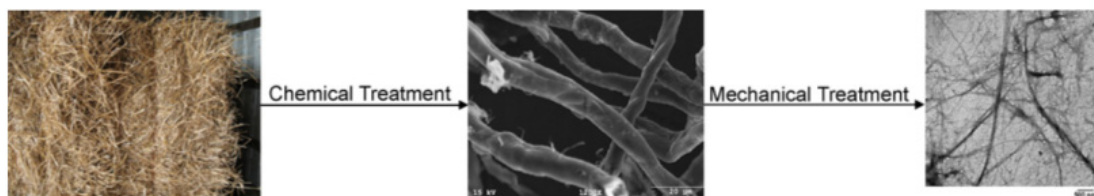


**Figure 7.** Images of natural wheat straw [57], wheat straw microfibers [54] after chemical treatment and wheat straw nanofibers [54] after chemical treatment.

## 2.8. Conventional chemical oxidative polymerization of aniline

Chemical oxidative polymerization of aniline is a traditional method for synthesizing polyaniline and during the early stages of this synthesis process polyaniline nanofibers are formed (Fig. 8). Optimization of polymerization conditions such as temperature, mixing speed, and mechanical agitation allows the end stage formation of polyaniline nanofibers with diameters in the range of 30–120 nm [58,59].

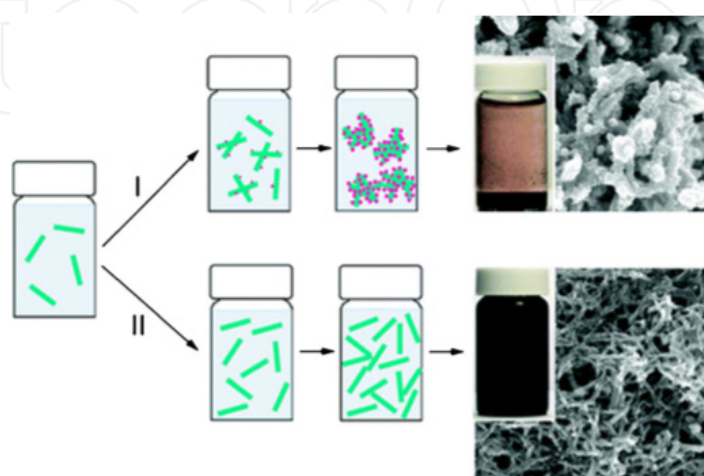


**Figure 8.** Schematic showing the nucleation of polyaniline nanofibers [59]. (I) Under non-ideal nucleation conditions aggregate formation is present. (II) When ideal nucleation conditions are predominant, well-dispersed polyaniline nanofibers are formed. Typical images of the reaction vials and microstructure are displayed next to the schematic.

## 2.9. Bacterial cellulose

Cellulose nanofibers produced by bacteria have been long used in a variety of applications, including biomedical applications [60]. Cellulose synthesis by *Acetobacter* involves the polymerization of glucose residues into chains, followed by the extracellular secretion, assembly and crystallization of the chains into hierarchically composed ribbons (Fig. 9). Networks of cellulose nanofibers with diameters less than 100nm are readily produced, and fibers with different characteristics may be produced by different strains of bacteria [49]. Copolymers have been produced by adding polymers to the growth media of the cellulose producing bacteria [50,51].

## 2.10. Kinetically controlled solution synthesis

Nanofibers and nanowires have been fabricated in solution using linear aligned substrates as templating agents such as iron-cation absorbed reverse cylindrical micelles and silver nanoparticles [61]. Poly(vinyl alcohol)-poly(methyl methacrylate) nanofibers were fabricated using silver nanoparticle that were linearly aligned in solution by vigorous magnetic stirring (Fig. 10) [62]. These nanoparticle chain assemblies acted as a template for further polymerization of nanofibers with diameters from 10 to 30 nm and lengths up to 60  $\mu\text{m}$ .



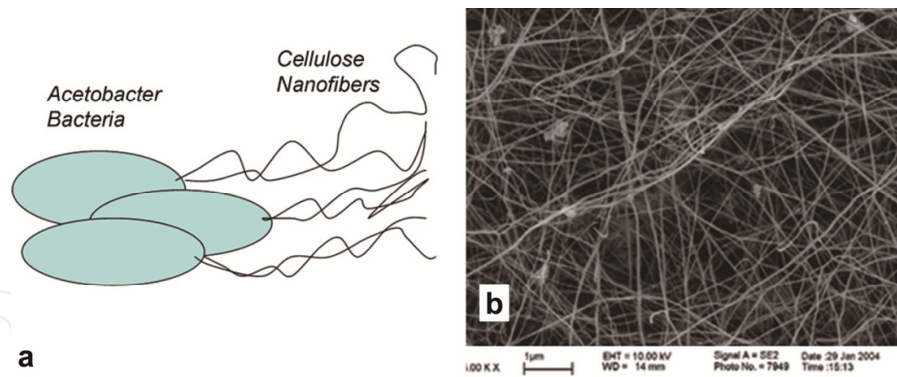


**Figure 9.** (a) Schematic of Acetobacter cells depositing cellulose nanofibers, (b) an SEM image of a cellulose nanofiber mesh produced by bacteria [60].

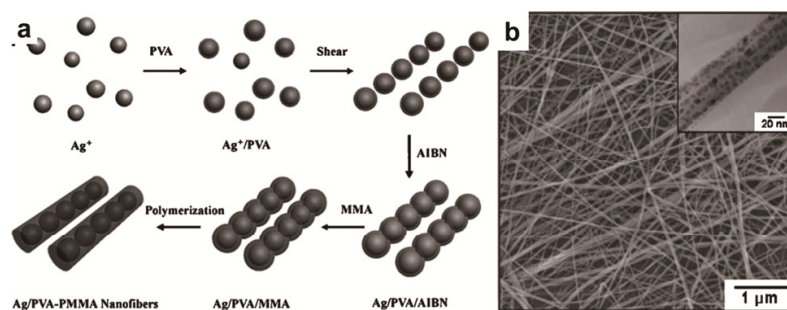


**Figure 10.** (a) Schematic of silver nanoparticle embedded polymer nanofibers fabrication (b) SEM and TEM images of silver nanoparticle embedded Polymer nanofibers [62].

### 3. Polymer MNF based photonic components and devices

Optical fiber based components and devices have been very successful in the past 30 years and will surely continue to thrive in a variety of applications including optical communications, optical sensing, power delivery and nonlinear optics [63-65]. With increasing requirements for higher performance, wider applicability and lower energy consumption, there is a strong demand for the miniaturization of fiber-optic components or devices. When operated on a smaller spatial scale, a photonic circuit can circulate, process and respond to optical signals on a smaller time scale. Only at wavelength or subwavelength size does the photonic structure manifest evident near-field features that can be utilized for interlinking and processing optical signals highly efficiently. For example, it was estimated that to reach an optical data transmission rate as high as 10 Tb/s, the size of photonic matrix switching devices should be reduced to 100-nm scale [66]. At the same time, to perform a given function that relies on a certain kind of light-matter interaction, usually less energy is required when smaller quantities of matter are involved. MNFs featured at subwavelength scale, provide a number of interesting properties such as mechanical flexibility, high optical cross-sections, large and ultrafast nonlinear responses, and broad spectral tunability that are highly desirable for functionalizing high density and miniaturized PICs [67]. Besides its low cost and tiny size, MNFs are also easy to couple with other general optical devices, providing excellent compatibility with standard optical fiber systems. This section gives an up-to-date review of polymer MNF based photonic components/devices that have been investigated very recently.

### 3.1. Polymer MNF-based passive components/devices

#### 3.1.1. $M \times N$ coupling photonic splitters and sensors

X. Xing et al. have demonstrated PTT nanofibers with high surface smoothness, diameter uniformity, as well as high mechanical strength and excellent flexibility, make them promising candidates for building blocks to construct ultracompact photonic devices and device arrays [17,18]. Fig.11a shows a 4×4 photonic coupling splitter assembled by twisting four PTT nanofibers with diameters of 450, 450, 510, and 570 nm for branches A to D [18]. The inset of Fig. 11a shows that the coupling section is composed of a 3×4 and a 1×4 couplers, where the total width of the coupling section is 1.98 μm. The maximum length of the coupling region is about 16.1 μm, and that for the 1×4 splitter is about 8.5 μm. When two red lights (650 nm) are simultaneously launched into the branches A and B, the measured splitting ratio is 29:18:29:24. As shown in Fig. 11b, blue light (532 nm) are coupled into the branch G of an 8×8 coupling splitters and divided into branches 1 to 8. The coupling section of the splitter (Fig. 11b, inset) is 38-μm-long and 2.5-μm-wide. We also launched other visible lights into the devices to observe the splitting phenomenon. Experimental demonstration shows that the properties of the splitters are dependent on the operation wavelength and the input branch which the optical signal launched into. For a fixed operation wavelength and the input branch, desirable splitting ratio can be tuned by controlling input/output branching angle.

As shown in Fig. 11c–e, a tunable refractive index sensor with ultracompact structure in a 2×2 PTT nanofiber coupling splitter assembled by twisting two flexible PTT nanowires with diameter of 400 nm [19]. The sensor consists of two input branches, a twisted coupling region, and two output branches. The changes of optical power caused due to variations in the surrounding medium around the twisted coupling region were measured in the output branches. The highest measured sensitivity of the sensor is 26.96 mW/RIU (refractive index unit) and the maximum detection limit on refractive index change is  $1.85 \times 10^{-7}$ .

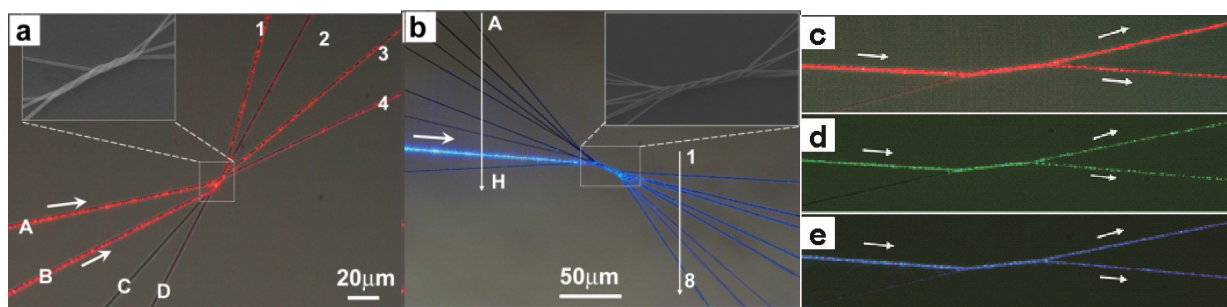


**Figure 11.** Optical microscope images [18,19]: (a) A 4×4 photonic coupling splitter with diameters of 450, 450, 510, and 570 nm for branches A to D when red light (650 nm) was launched into branches of A and B. (b) An 8×8 photonic coupling splitter of guided blue light (532 nm) with diameters of 400, 400, 400, 400, 400, 750, 750, and 600 nm for branches A to H. The inset of Fig. a and b shows the coupling section of devices. (c–e) the sensor (400-nm-diameter) taken with (c) red light, (d) green light (532 nm), and (e) blue light (473 nm) (without sample solution). The white arrows show the propagation directions of the launched lights.

### 3.1.2. Cascaded MZI[21]

Figure 12 shows an optical microscope image of the assembled two-cascaded MZI (wire diameter, 900 nm) [21]. The inset (a) shows a scanning electron microscope image of MZI 1 and the inset (b) shows guided red light (650 nm) in the cascaded MZI. The measured insertion loss is about 0.94 dB for the red light. The total length of the cascaded MZI is 327  $\mu\text{m}$ . The width and length of each bow-shaped MZI are 32  $\mu\text{m}$  and 121  $\mu\text{m}$ , respectively. According to the analysis, to get coupling ratios of 0.147, 0.501, and 0.147, the lengths of the couplers  $C_1$ ,  $C_2$ , and  $C_3$  are 27, 31, and 27  $\mu\text{m}$ , respectively. The estimated total path-length difference is 40  $\mu\text{m}$ . The bright spot in the inset (b) of Fig. 12 is the scattering spot of the input light at the end of the tapered fiber I. The average bandwidth of 3-dB pass-band is measured to 33 nm for the cascaded MZI over the wavelengths of 1.3 to 1.6  $\mu\text{m}$ . The measured extinction ratio for the cascaded MZI is 16 to 19 dB, and optical insertion loss is 1.1 to 1.8 dB at wavelengths of 1.3 to 1.6  $\mu\text{m}$ . This is good for band-pass filter applications.

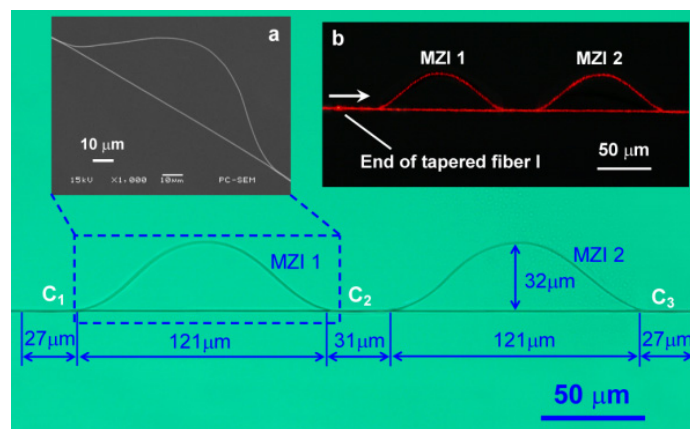


**Figure 12.** Optical microscope image of the assembled cascaded MZI (wire diameter, 900 nm) [21]. Inset (a) shows the scanning electron microscope image of bow-shaped MZI 1 and inset (b) shows the optical microscope image of guided red light (650 nm) in the cascaded MZI. Estimated path-length difference is 40  $\mu\text{m}$ . The white arrow in the inset (b) indicates propagation direction of the light.

### 3.1.3. Ring resonator[31]

Owing to relatively high quality (Q) factor and ease of fabrication, fiber-based microrings were widely used for resonators. Y. Wang et al. have assembled microring resonators by knotting a uniform PTT wire with micromanipulator assistance under an optical microscope. Subsequently, two ends of the microring resonator were fixed on two branches of a tunable microstage as schematically shown in Fig. 13a. Then an input microtaper and an output microtaper were used to launch and collect optical signals, respectively, by evanescent wave coupling. In Fig. 13a, when we adjust the tunable microstage to the right, the wire will be pulled tightly and finally, the ring radius will become smaller. The red arrows in Fig. 13a show the propagation directions of the optical signals while the yellow one indicates the moving direction of the tunable stage. As an example, Fig. 13b shows a SEM image of the microring with a radius of 70  $\mu\text{m}$ , which was assembled by the PTT wire with a diameter of 3.5  $\mu\text{m}$ .

Three tunable microrings were assembled by PTT wire with diameters of 3.5, 2.5, and 2.0  $\mu\text{m}$ , respectively. Ring radius and wire diameter dependent optical properties were demonstrated by measuring the FSRs and the Q factors and showed that, the maximum Q factors are 28090, 28071, and 23528 at the ring radii of 417 (wire diameter, 3.5  $\mu\text{m}$ ), 258 (wire diameter, 2.5  $\mu\text{m}$ ), and 204 (wire diameter, 2.0  $\mu\text{m}$ )  $\mu\text{m}$ , respectively. Their corresponding FSRs are 0.55, 0.92, and 1.19 nm. The FSR is mainly dependent on the ring radius and little affected by the wire diameter. By using an appropriate wire diameter with an appropriate ring radius, a maximum Q can be obtained with a desirable FSR. The tunable microring resonators would be useful for optical filters and sensors. Also, the assembly method used in this work could become a candidate for fabricating highly-integrated photonic devices based on micro/nano-wire rings.

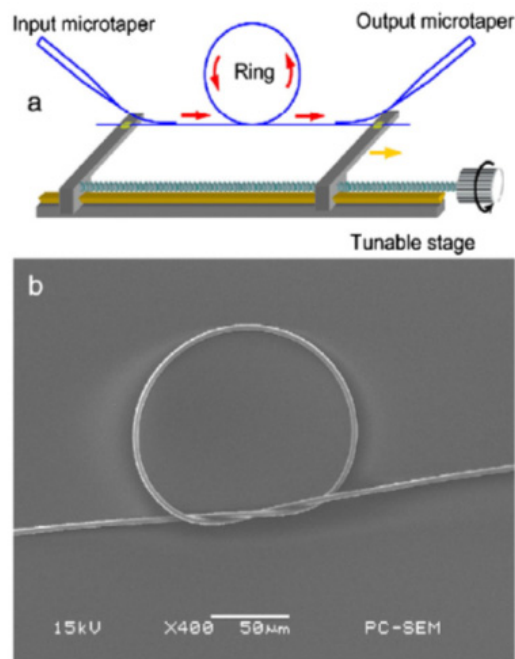


**Figure 13.** (a) Schematic illustration of the experimental setup. The red arrows show propagation directions of the optical signals whereas the yellow one indicates moving direction of the tunable stage. (b) SEM image of a microring assembled by the PTT wire. The wire diameter is 3.5  $\mu\text{m}$  and the ring radius is 70  $\mu\text{m}$  [31].

#### 3.1.4. Arbitrary and vertical optical couplers using flexible polymer MNFs[32]

The polymer MNFs were directly drawn from a polymethyl methacrylate (PMMA) solution in which acetone was used as a solvent. To investigate the possibility of arbitrary and vertical optical couplers, different topologies were assembled. Figures 14a, b show the optical microscope images of two crossed interconnect structures with different cross angles. The structure of Fig. 14a as assembled by two polymer fibers with diameters of 1.05  $\mu\text{m}$  (wire 1) and 1.00  $\mu\text{m}$  (wire 2). Cross angle between channels  $C_1$  and  $C_2$  is  $57^\circ$  while the cross angle between channels  $C_3$  and  $C_4$  is  $42^\circ$ . Figure 14a shows that a light (wavelength  $\lambda=650$  nm) was launched into channel  $C_1$  and divided into channels  $C_2$ ,  $C_3$ , and  $C_4$ . The output powers were collected using the tapered fibers. For this structure, 4% optical power was divided into channel  $C_2$ . The powers divided into channels  $C_3$  and  $C_4$  are 41% and 42%,



respectively. The total insertion loss is 0.6 dB. Figure 14b further shows a crossed interconnect structure, which was assembled by two wires with diameters of 1.18  $\mu\text{m}$  (wire 1) and 1.40  $\mu\text{m}$  (wire 2). The cross angle between channels  $C_1$  and  $C_2$  is  $55^\circ$  and that between channels  $C_3$  and  $C_4$  is  $89^\circ$ . For this structure, when the light ( $\lambda=650$  nm) was launched into channel  $C_1$ , the measured powers at channels  $C_2$ ,  $C_3$ , and  $C_4$  are 1%, 39%, and 42%, respectively. The total insertion loss is 0.86 dB. Figure 14c shows the optical microscope image of the star topology network with five channels. It was assembled by twisting three wires with diameters of 1.08  $\mu\text{m}$  (wire 1), 917 nm (wire 2), and 970 nm (wire 3). The cross angle between channels  $C_1$  and  $C_2$  is  $29^\circ$ , that between channels  $C_2$  and  $C_3$  is  $57^\circ$ , between channels  $C_3$  and  $C_4$  is  $110^\circ$ , and between channels  $C_4$  and  $C_5$  is  $35^\circ$ . When the light ( $\lambda = 650$  nm) was launched into channel  $C_2$ , the measured powers in the channels  $C_3$ ,  $C_4$ , and  $C_5$  are 1%, 40%, and 36%, respectively. The total insertion loss is 1.14 dB. Figure 14d shows a tree topology network, which was assembled by three wires with diameters of 1.17  $\mu\text{m}$  (wire 1), 1.37  $\mu\text{m}$  (wire 2), and 1.20  $\mu\text{m}$  (wire 3). The cross angle between channels  $C_1$  and  $C_3$  is  $87^\circ$  and that between channels  $C_4$  and  $C_5$  is  $39^\circ$ . When the light ( $\lambda = 650$  nm) was launched into channel  $C_2$ , it was divided into channels  $C_1$  and  $C_3$  by the first node A with a splitting power ratio of 0.41:0.40. At the second node B, the light in channel  $C_3$  was divided into channels  $C_4$  and  $C_5$  with a splitting power ratio of 0.16:0.17. The total insertion loss for this structure is 1.31 dB. By using the structures shown in Figs. 14a–c, optical channels can be further increased while keeping one node. This is very useful for ultracompact arbitrary and vertical optical interconnect structures. We hope that the arbitrary and vertical coupling structures could find applications in high-density PICs and miniaturized optical networks.

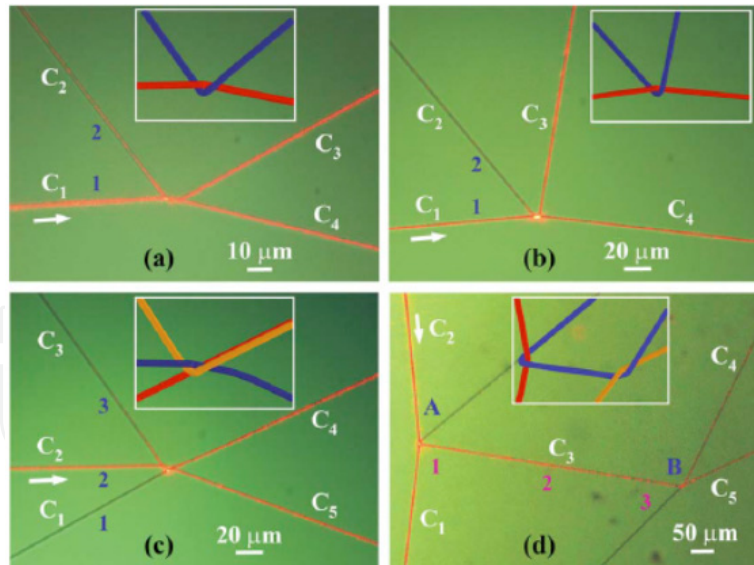


**Figure 14.** Optical microscope images of different arbitrary and vertical optical couplers [32]. The insets schematically represent respective structures, and the white arrows indicate the transmission direction of the guided light. (a) Optical microscope image of a crossed interconnect structure assembled by wires 1 and 2 with diameters of 1.05 and 1.00  $\mu\text{m}$ , respectively. (b) Optical microscope image of a crossed interconnect structure assembled by wires 1 and 2 with diameters of 1.18 and 1.40  $\mu\text{m}$ , respectively. (c) Optical microscope image of a star topology network assembled by three wires with diameters of 1.08  $\mu\text{m}$  (wire 1), 917 nm (wire 2), and 970 nm (wire 3). (d) Optical microscope image of a tree topology network assembled by three wires with diameters of 1.17  $\mu\text{m}$  (wire 1), 1.37  $\mu\text{m}$  (wire 2), and 1.20  $\mu\text{m}$  (wire 3).

### 3.2. Polymer MNFs as active waveguides

The development of miniaturized PICs are challenging directions in next generation all-optical signal processing, in which light-emitting sources are important elements for integration [68,69]. In the past decades, doped glass optical fibers have been widely used as solid hosts for photonic applications such as tunable lasers and amplifiers for optical communication [70,71]. For most widely used rare-earth-doped glass fibers, the concentrations of rare-earth dopants are limited by the concentration quenching, for example, typically lower than 1% for  $\text{Er}^{3+}$  in silica fibers, resulting in relatively low energy conversion efficiency within a limited length. Therefore, it is difficult to obtain efficient energy conversion in doped glass fibers within a scale comparable to the compactness of a nanophotonic integrated system. Compared to those of glass fibers, the most attractive prospects of polymer MNFs are as follows: First, the polymer matrix can host functional dopants ranging from metal oxides, quantum dots (QDs), and fluorescent dyes to enzymes that can be used to tailor the properties of the MNFs with greater versatility. Second, the dopants can be easily doped into the solvated polymer and drawn into polymer MNFs at room temperature with higher doping concentration than that in glass fibers. Also, the mechanical flexibility, perm-selective nature to gas molecules, biocompatibility, easy processing, and low cost of the polymer materials [72] offers more opportunities for doped polymer MNFs over doped glass fibers in nanophotonic systems. Especially, high efficient light emission dopants (e.g., fluorescent dyes and QDs), which are much more compatible with polymer MNFs, show great potential to realize compact light-emitting sources with feature sizes acceptable in nanophotonic integrated systems.

#### 3.2.1. Fluorescent dye doped polymer MNFs

In 2010, F. Gu et al. reported light-emitting polymer nanofibers based on waveguiding excitation [34]. By waveguiding excitation light along the polymer nanofiber, the interaction of light with polymer nanofiber is enhanced over 3 orders of magnitude compared with the currently used irradiating excitation. Intriguing advantages such as enhanced excitation efficiency, low excitation power operation down to nW levels, tightly confined excitation with low cross talk, and high photostability of the light-emitting polymer nanofibers are obtained. The waveguiding excitation allows incorporation of various fluorescent dyes into polymer nanofibers to generate multicolor emitting sources covering the entire visible spectrum.

Figure 15a shows a photoluminescence (PL) microscope image of a 380-nm-diameter 520- $\mu\text{m}$ -length RhB-PS nanofiber taken with a long-pass emission filter [34]. Upon 473-nm laser ( $\lambda_{\text{ex}}$ ) launched from the left side with excitation power ( $P_{\text{ex}}$ ) of 70 nW, bright fluorescent emission with a peak ( $\lambda_{\text{em}}$ ) around 578 nm is generated and guided along the nanofiber. For reference, Fig. 15b shows the PL image taken without the emission filter, in which a small light spot at the output end of the nanofiber and no obvious scattering along the nanofiber are observed, suggesting that the excitation light was efficiently absorbed during its

waveguiding excitation. The absorption spectrum of the RhB-PS nanofiber in Fig. 15c (black line) exhibits a peak at 560 nm due to the absorption of the doped RhB molecules. The measured absorption coefficient  $\alpha$  of the RhB-PS NFs at 473 nm is  $\sim 50 \text{ cm}^{-1}$ .

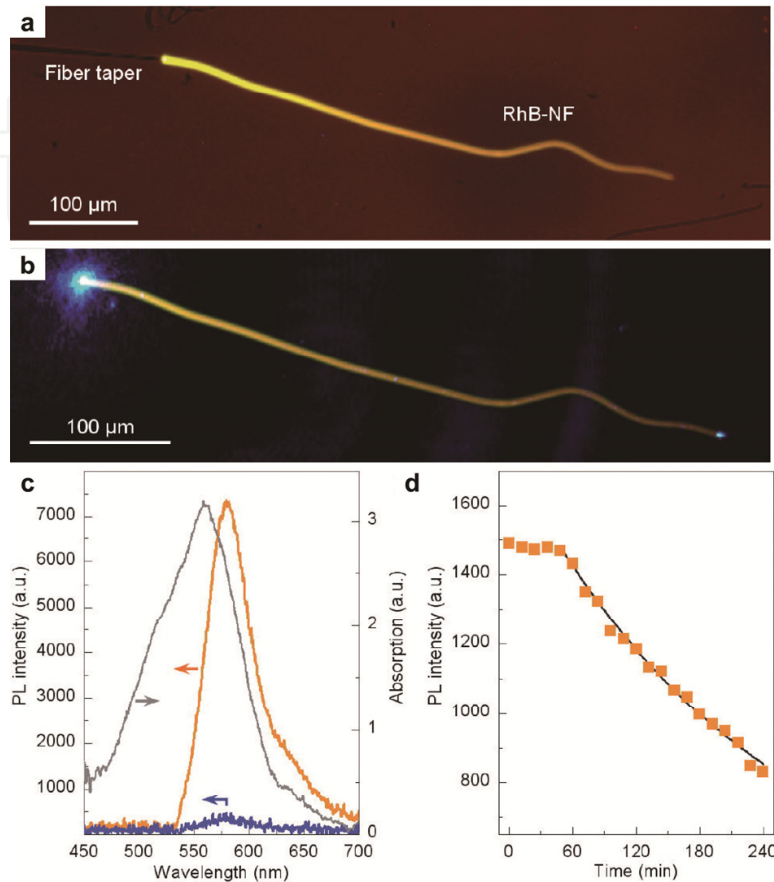


**Figure 15.** PL microscope images of a 380-nm-diameter 520- $\mu\text{m}$ -length RhB-PS nanofiber excited by 473-nm light from the left side at  $P_{\text{ex}} = 70 \text{ nW}$ , taken with (a) and without (b) the long-pass emission filter. (c) PL spectra of the RhB-PS nanofiber under 70-nW waveguiding (orange line) and 3- $\mu\text{W}$  irradiation (blue line) schemes. The absorption spectrum of the NF is also provided (black line). (d) PL intensity of the RhB-PS nanofiber at 579 nm with  $P_{\text{ex}} = 30 \text{ nW}$  as a function of time [34].

### 3.2.2. Quantum-dot-doped Polymer MNFs

H. Liu et al. incorporated semiconductor QDs as integrated light sources into the polymer fiber to produce subwavelength-diameter optical waveguides [16]. Fibers of polymeric photoresist were fabricated with diameters down to 50 nm and lengths up to tens of millimeters using an electrospinning method, and QDs consisting of CdSe/ZnS (core/shell) were incorporated into the polymer fibers. A fluorescence optical image (Fig. 16a), taken by uniformly illuminating the fiber by a mercury lamp light source and imaging the 605 nm wavelength fluorescence, shows the distribution of luminescence along the fiber length. The image suggests that the QDs were not uniformly distributed along the fiber. Nanometer-sized QDs were clearly recognizable, and were observed to be concentrated in a constrained region as a strand parallel to the fiber axis (Fig. 16b).

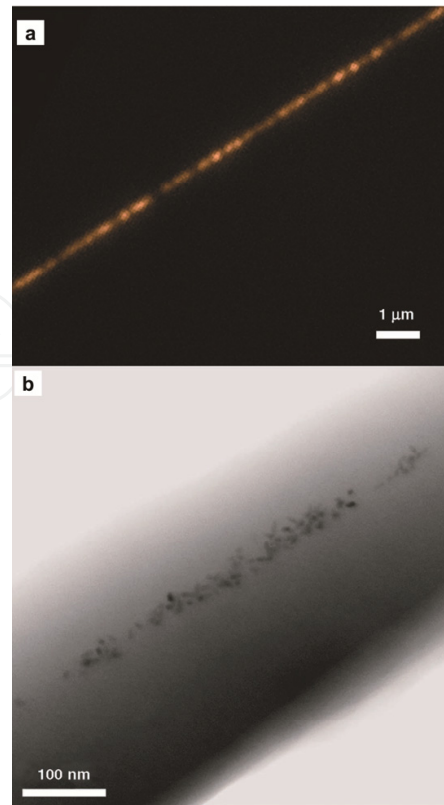


**Figure 16.** QD distribution in the SU8 nanofiber [16]: a) Fluorescence image of ensembles of QDs embedded in an SU8 nanofiber, showing the distribution of luminescence along the fiber length. b) TEM image of QD distribution inside the SU8 nanofiber.

### 3.2.3. QD-Decorated Polymer MNFs

H. Yu et al. developed a one-step process to decorate PTT nanofiber with the CdSe/ZnS core/shell QDs [73]. The QDs-decorated nanofibers with diameters of 400–800 nm can be used as active subwavelength waveguides with some advantages such as good photostability, low excitation power operation (less than 0.2  $\mu\text{W}$ ), low propagation loss (11.3 dB/cm), low absorption coefficient (down to 2.6  $\text{cm}^{-1}$ ), and 200 times enhancement in excitation efficiency excited by the evanescent waveguiding excitation than that of by the irradiation excitation.

Figure 17a shows an optical microscope image of a drop of a rugby-ball-like QDs-decorated cross structure, composing of a PTT nanofiber 1 (495 nm) and a PTT nanofiber 2 (590 nm), excited by the EW excitation from laser B at  $P_{\text{ex}} = 0.1 \mu\text{W}$ . It can be seen that red light was excited in the rugby-ball-like QDs. Figure 17b shows the optical microscope image of the cascaded rugby-ball-like QDs-decorated nanofiber with diameter of 597 nm, in which there are seven rugby-ball-like QDs. The lengths of the QDs B<sub>1</sub> to B<sub>7</sub> are 2.3, 2.2, 2.3, 2.2, 1.8, 2.0, and 2.0  $\mu\text{m}$ , respectively. Their corresponding maximum widths are 1.6, 1.5, 1.6, 1.6, 1.0, 1.1, and 1.1  $\mu\text{m}$ . The average length of the rugby-ball-like QDs is 2.1  $\mu\text{m}$  and the average value of maximum width is 1.4  $\mu\text{m}$ . Figure 17c shows the corresponding optical microscope image with seven red spots excited by the 473 nm blue light from laser B at  $P_{\text{ex}} = 1.2 \mu\text{W}$ .



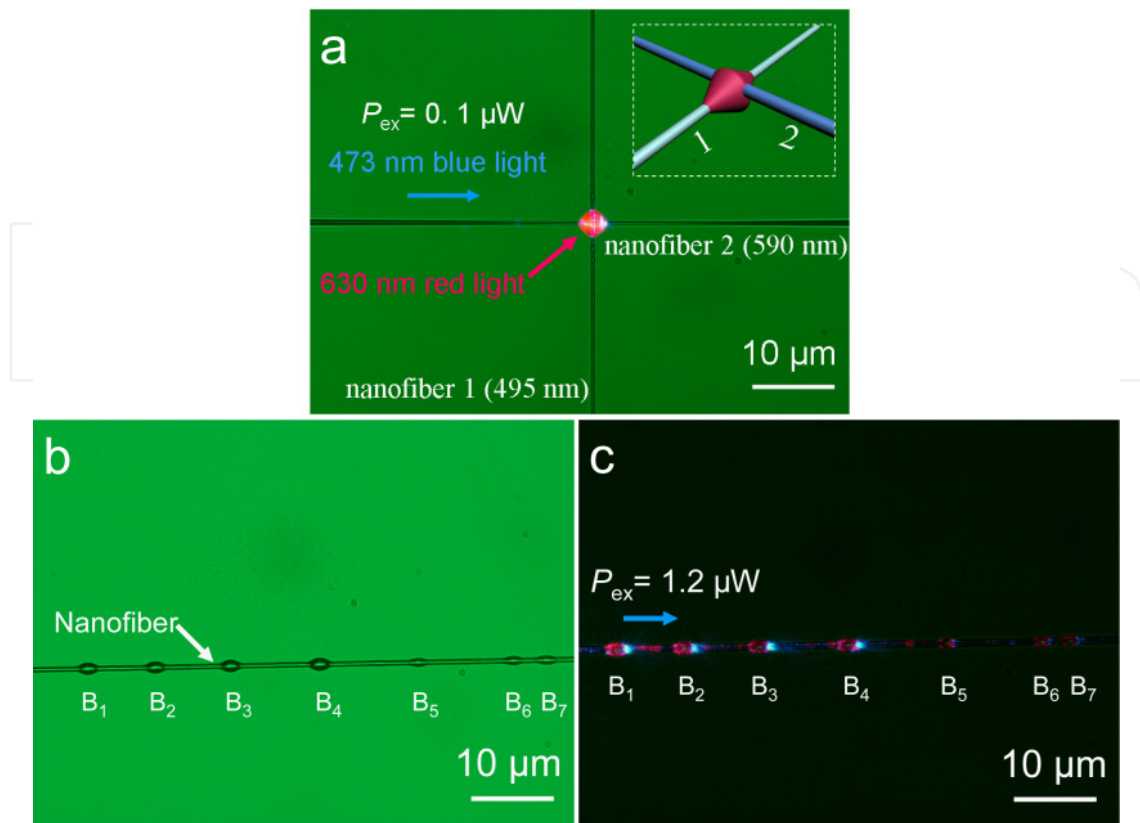


**Figure 17.** Optical microscope images of nanofibers with a rugby-ball-like QDs-decorated cross structure and a cascaded rugby-ball-like QDs-decorated structure [73]. (a) Crossed structure with a guided 473 nm blue light in nanofiber 2 and excited 630 nm red light at the cross junction. The inset schematically represents the cross structures. (b) Cascaded rugby-ball-like QDs-decorated structure. The lengths of the QDs B<sub>1</sub> to B<sub>7</sub> are 2.3, 2.2, 2.3, 2.2, 1.8, 2.0, and 2.0 μm, respectively. The corresponding maximum widths are 1.6, 1.5, 1.6, 1.6, 1.0, 1.1, and 1.1 μm. (c) Rugby-ball-like QDs-decorated fiber excited by 473 nm blue light at  $P_{ex} = 1.2 \mu W$ . The blue arrow shows the direction of propagation of the input blue light.

### 3.3. Polymer nanofiber laser

#### 3.3.1. Dye Doped Polymer MNF Knot Resonator Laser

Recently, many kinds of microsized polymer fiber and dye doped polymer fiber were also successfully demonstrated. Q. Song et al. reported the lasing action in a dye doped PNF knot ring resonator [74]. The dye doped polymer nanofiber was fabricated by general fiber drawing technique. Then it was bent to a knot ring resonator and fixed onto glass tubes (the inset of Fig. 18a), which can increase the stability of the knot resonator and fix its diameter [74]. Laser emission was observed. The emission spectrum of knot resonator is shown in Fig. 18b. Here the pump intensity is 4.2 mJ/cm<sup>2</sup>. Periodic peaks can be observed in the laser spectrum. This group of peaks is considered to come from the whispering gallery mode resonance inside the ring resonator. The linewidth of laser peaks is only 0.07 nm and the mode spacing in Fig. 18 is about 0.206 nm.

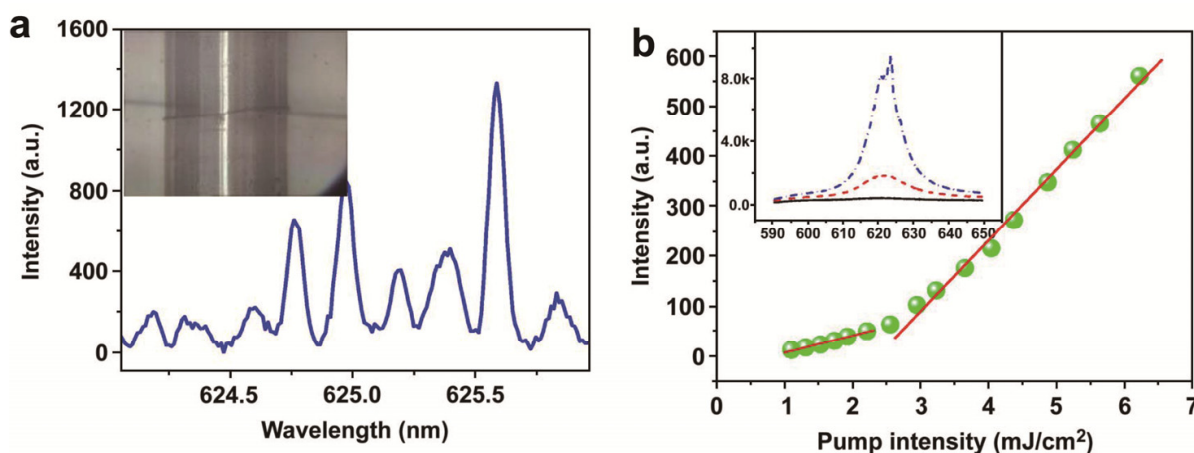


**Figure 18.** Laser spectrum of dye doped polymer fiber [74].

### 3.3.2. Random lasing in a single organic Nanofiber

One-dimensional light random lasing in individual p-sexiphenyl nanofibers (p-6P) is investigated by F. Quochi et al [36]. The laser action happens in single p-6P nanofibers grown on (001)-oriented muscovite mica. Isolated nanofibers are shown to yield low-threshold random laser emission in the deep blue. Random lasing from isolated nanofibers starts at pump fluences on the order of  $10 \mu\text{J}/\text{cm}^2$  per pulse. Lasing nanofibers are demonstrated. Figure 19a shows a lasing micrograph taken in imaging mode slightly above threshold. It displays both lasing from vertically aligned nanofibers and spontaneous emission from a set of neighboring nanofibers oriented approximately at  $60^\circ$  with respect to the vertical axis of the detection system. The latter faintly appear in the lower part of the graph. Scattering of the lasing emission into out-of-plane directions does not take place homogeneously along the nanofibers' axis; conversely, scattering is highly spotted, indicating that wave-guiding is interleaved with light scattering and outcoupling at special sites along the fibers. Emission spectra relating to the  $\sim 100 \mu\text{m}$  long nanofiber placed at the center of the imaging field of view in Fig. 19a are reported in Fig. 19b. They refer to the emission spatially integrated over the whole nanofiber length. Below threshold, spontaneous emission exhibits a broad vibronic progression with 0–1 and 0–2 emission bands peaked near 425 and 450 nm, respectively.

### 3.3.3. Optically pumped lasing in single conjugated polymer nanowires

Conjugated polymers have chemically tuneable opto-electronic properties and are easily processed, making them attractive materials for photonics applications [75,76]. Conjugated polymer lasers, in a variety of resonator geometries such as microcavity, micro-ring, distributed feedback and photonic bandgap structures, have been fabricated using a range of coating and imprinting techniques [77-80]. D. O'Carroll et al. reported the first observation of optically pumped lasing in single conjugated polymer nanowires [81]. The waveguide and resonator properties of each wire are characterized in the far optical field at room temperature. The end faces of the nanowire are optically flat and the nanowire acts as

a cylindrical optical cavity, exhibiting axial Fabry–Pérot mode structure in the emission spectrum. Above a threshold incident pump energy, the emission spectrum collapses to a single, sharp peak with an instrument-limited line width that is characteristic of single-mode excitonic laser action. Fluorene-based conjugated polymers are attractive.

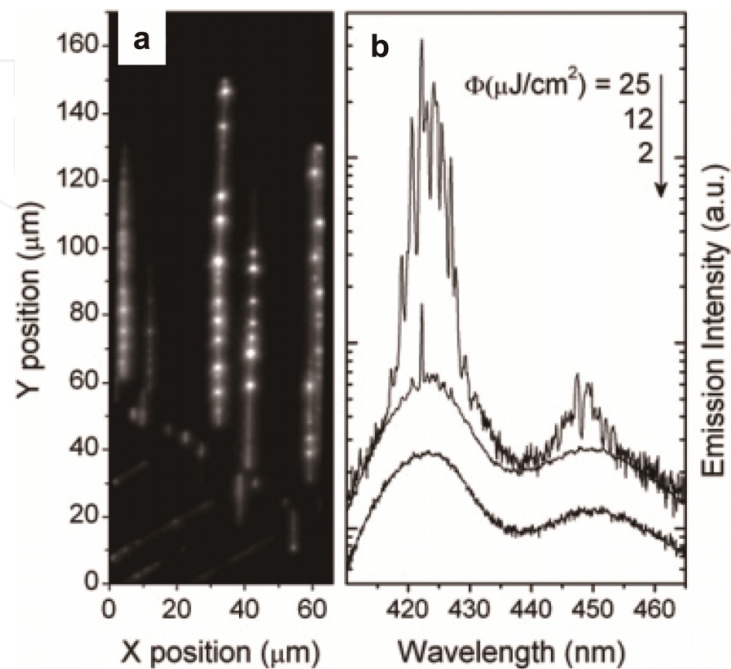


**Figure 19.** (a) Gray-scale optical emission intensity image of lasing and luminescent *p*-6P nanofibers excited at a pump fluence ( $\Phi$ ) of  $15 \mu\text{J}/\text{cm}^2$  per pulse. The gray-level scale is logarithmic. The  $y$  coordinate refers to the position along the vertical direction, which is parallel to the input slit of the detection system. (b) Emission intensity spectra of the nanofiber positioned at  $x \approx 30 \mu\text{m}$  in panel a and extending vertically from  $y \approx 50 \mu\text{m}$  to  $y \approx 150 \mu\text{m}$  for different values of the pump fluence. Note that the threshold fluence is lower than  $12 \mu\text{J}/\text{cm}^2$  per pulse [36].

Fluorene-based conjugated polymers are attractive photonic materials because they exhibit high photoluminescence quantum efficiencies, large stimulated emission crosssections and chemically tuneable emission wavelengths [82]. Poly(9,9-dioctylfluorene) (PFO) is a prototypical main-chain liquid-crystalline homopolymer that emits in the blue and exhibits polymorphic behaviour, with striking implications for its photophysical properties [83]. Isolated PFO nanowires were uniformly excited by the 355-nm output of a 0.7 ns, 1.25 kHz pulsed Nd/YVO laser and spatially resolved photoluminescence spectra were acquired from the bodies and tips (Fig. 20a). To confirm that the wires operated as axial Fabry–Pérot microcavities, the mode spacing at 460 nm was plotted versus the inverse nanowire length for 14 wires, and was shown to exhibit a linear dependence (Fig. 20b). The number of Fabry–Pérot modes per guided mode that could propagate in a nanowire microcavity was estimated from  $\Delta\lambda_{\text{spont}}/\Delta\lambda_m$ , where  $\Delta\lambda_{\text{spont}}$  is the full-width-at-half-maximum, FWHM, of the spontaneous emission and is  $\sim 19$  nm.

Single isolated PFO nanowire microcavities were then uniformly excited (355 nm, 0.7 ns, 1.25 kHz) and tip emission spectra were collected as a function of pump energy (Fig. 21a).

At lower pump energies, tip spectra exhibited nanowire microcavity emission, with pronounced Fabry–Pérot modes apparent at the 0–1 peak. Above an energy threshold of  $\sim 100$  nJ ( $2.8$  mJ cm $^{-2}$ ), a single spectrally narrowed emission peak developed by preferential gain in a single Fabry–Pérot mode and the onset of lasing. A slight blue shift in peak position with increasing pump energy suggested that stimulated emission occurred on timescales comparable to or faster than exciton energy migration. Concerning the dependence of tip emission intensity on pump energy, below the energy threshold, emission increased linearly with excitation energy (Fig. 21b). Above threshold, a kink in emission output was followed by a super-linear increase due to optical gain. Also, the emission peak width narrowed from 19.6 nm to 1.4 nm (instrument-limited) at threshold, indicating the high quality factor of the nanowire cavity.

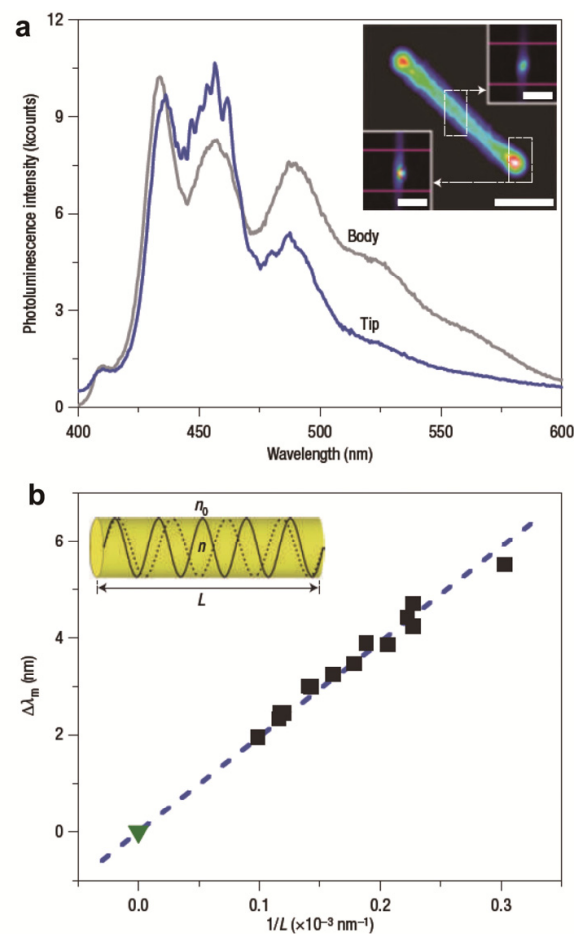


**Figure 20.** Microcavity effects in single PFO nanowires [81]. a, Emission spectra collected from the tip (blue) and body (grey) of an isolated PFO nanowire under uniform pulsed excitation (1.4 nJ). Inset: emission image of an excited wire (1nJ) with spatially filtered emission images of the tip and body locations from which spectral data were acquired; mauve lines indicate the area over which each spectrum was integrated. Scale bars, 2  $\mu$ m. b, Plot of mode spacing measured at 460 nm versus inverse nanowire length for 14 different nanowires. Black squares, experimental data points; green triangle, extrapolation to infinite length; dashed blue line, fit of Fabry–Pérot equation to data for  $\lambda = 460$  nm and  $[n - \lambda(dn/d\lambda)] = 5.4$ . Inset: schematic depiction of a nanowire with well-defined end facets acting as a Fabry–Pérot microcavity.



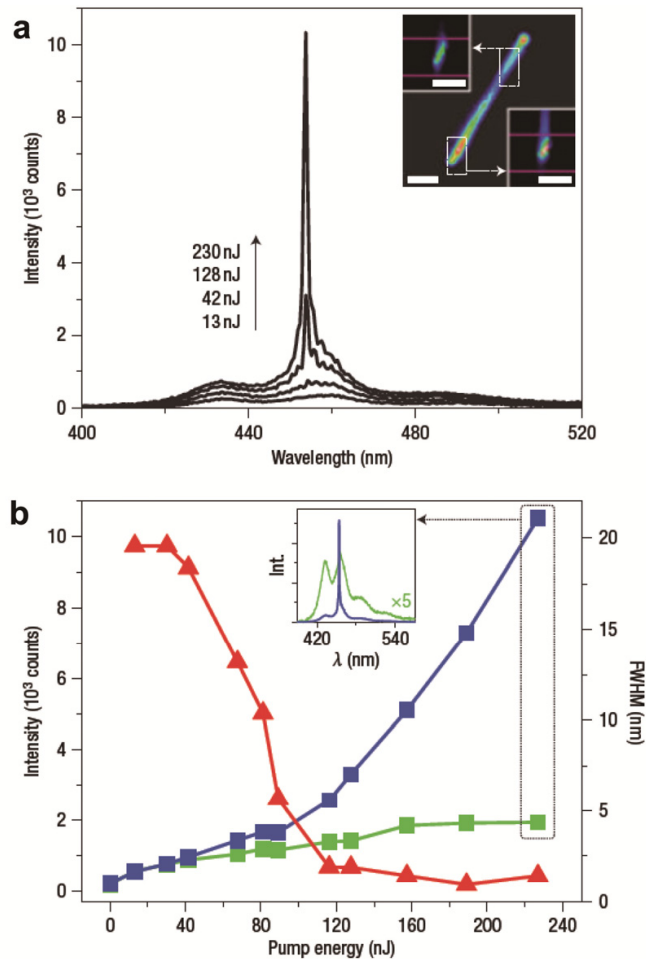


**Figure 21.** Optically pumped single PFO nanowire laser [81]. a, Emission spectra collected from the tip of an isolated PFO nanowire under uniform excitation, as a function of increasing pump energy at room temperature. Inset: emission image of the wire (1.3 nJ) along with spatially filtered emission images of the tip and body locations from which spectral data were acquired. Scale bars, 2  $\mu\text{m}$ . b, Plot of the tip emission peak intensity (blue squares) and FWHM (red triangles) versus pump energy for the wire shown in a. The intensity of emission from the nanowire body (green squares) is low and almost linear with pump energy. Solid symbols correspond to experimental data points and lines are guides to the eye. Inset: above threshold (230 nJ) emission spectra acquired from the wire tip (blue) and body (green).

### 3.4. Polymer nanofiber photodetector

Semiconducting polymers are attractive materials due to their chemically tunable optical and electronic properties, as well as their facility for solution processing [84,85]. Garret A. O'Brien et al. have demonstrated that solution-assisted template wetting may be successfully exploited for high-yield controlled synthesis of poly[(9,9-dioctylfluorenyl-2,7-diyl)-co-(bithiophene)] (F8T2) nanofibers and employed single nanowire devices as ultraminiature photodetectors. [35] Discrete nanowires with average lengths of 15  $\mu\text{m}$  and mean diameters of 200 nm has been fabricated. As expected, structural data point to a low degree of crystallinity within the wires. Individual nanowires can be electrically interfaced using either bottom- or top-contact geometries. Top-contacted single-nanowire devices with interelectrode gaps of approximately 5  $\mu\text{m}$  were fabricated on glass substrates using shadow masking and gold evaporation, see

Fig. 22a. The blue curve in Figure 22b shows the measured dark current ( $I_{\text{dark}}$ ) for a typical device. The data show quasilinear characteristics at low bias, similar to measured data for bottom-contacted nanowires, with some asymmetry at higher bias. The red curve in Fig. 22b shows the measured current ( $I_{\text{illum}}$ ) under continuous 405 nm illumination. A marked increase in the measured current is observed across the entire bias range. The green curve in Fig. 22b shows the measured current under manually chopped 405 nm illumination, where the illumination was switched on or off at 10 V intervals during the bias sweep, corresponding to a duty cycle of 50 %. The present photoconductivity measurements of F8T2 nanowire devices, which yield single-nanowire responsivities of approximately  $0.4 \text{ mA W}^{-1}$  and external quantum efficiencies of approximately 0.1% under monochromatic illumination; these values are comparable with data reported for single-inorganic-nanowire devices. The results demonstrate the promise of these novel nanostructures as ultraminiature photodetectors with the potential for integration into future hybrid nanophotonic devices and systems.

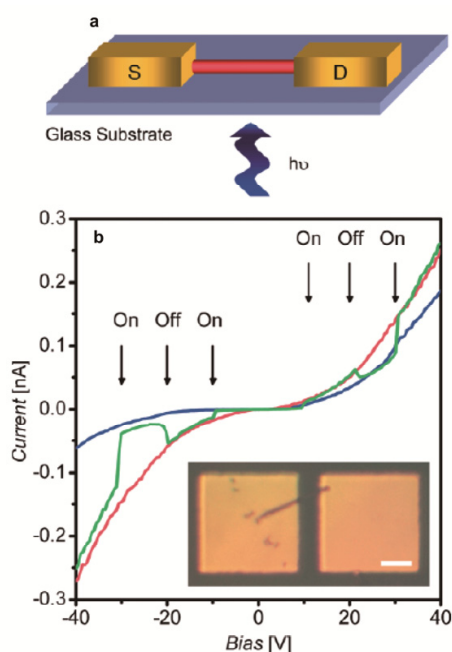


**Figure 22.** a) Schematic of a top-contact nanowire device. b) I–V characteristics of a top-contacted F8T2 nanowire acquired in the dark (blue line) and under 405 nm illumination (red line). Reversible switching in I–V data measured under manually chopped 405 nm illumination is also shown (green line). Inset: optical microscopy image of a typical top-contacted F8T2 nanowire device. Scale bar: 10  $\mu\text{m}$ . [35]

### 3.5. Nanopatterning of single light-emitting polymer nanofibres

Polymer nanofibers are compatible with sub-micrometre patterning capability and electromagnetic confinement within subwavelength volumes [2,86], they can offer the benefits of organic light sources to nanoscale optics. F. D. Benedetto et al. reported on the optical properties of fully conjugated, electrospun polymer nanofibres, demonstrated the enhancement of the fibre forward emission through imprinting periodic nanostructures using room-temperature nanoimprint lithography, and investigate the angular dispersion of differently polarized emitted light [87]. Fibers with diameters intentionally produced to be

in the range 0.5–5  $\mu\text{m}$  are used to collect reliable fluorescence micrographs and photoluminescence spectra. Confocal microscopy (Fig. 23a) on nanopatterned fibres shows uniformly bright imprinted gratings. The spectra of a typical poly[2-methoxy-5-(2-ethylhexyloxy)-1,4-phenylenevinylene] (MEH-PPV) fibre are displayed in Fig. 23b. In the emission of the untextured fibre the two replicas exhibit almost the same relative intensity, that is, a relative decrease of the high-energy spectral component ( $\lambda < 600$  nm). Different angular dispersion for light with s- and p-polarization, namely with the electrical field vector parallel or perpendicular to the grating grooves and corresponding to transversal electric (TE) or transversal magnetic (TM) guided modes, is demonstrated in Fig. 23c, respectively. The two modes are concomitantly present in the Bragg outcoupled emission, with TM peaks blueshifted by 18–46 meV with respect to the TE peaks, indicating a lower effective refractive index ( $n_{\text{eff}}$ ) for light polarized perpendicularly to the nanoimprinted features. For an MEH-PPV nanopatterned fibre,  $n_{\text{eff}}$  for TM and TE light monotonously decreases from  $\sim 1.9$  to 1.2 upon increasing the wavelength from 570 to 575 nm, whereas the difference,  $\Delta n_{\text{eff}} = n_{\text{eff,TE}} - n_{\text{eff,TM}}$ , slightly increases from 0.01 to 0.04 (Fig. 23d).

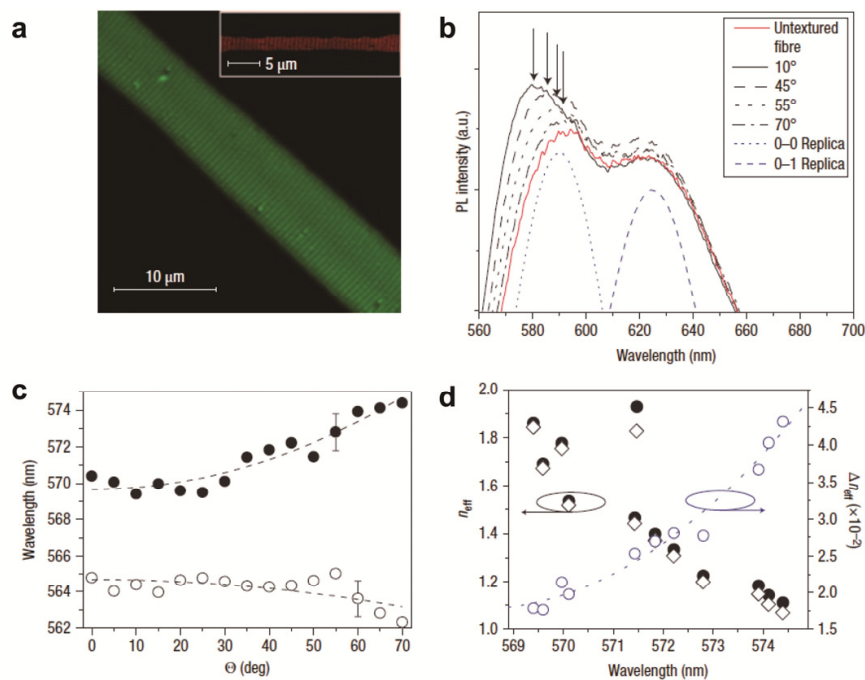


**Figure 23.** Emission properties of nanopatterned fibres [87]. a, Confocal microscopy pictures of nanoimprinted fibres. The grating period varies from 520 nm (green GE fibre from 1:8 dimethyl formamide:chloroform solution) to 640 nm (red MEH-PPV fibre from 1:5 dimethyl formamide:chloroform solution, inset). The GE fibre was imaged under two-photon excitation at  $\lambda = 800$  nm. b, Normalized angle-resolved photoluminescence spectra of an unpatterned and nanoimprinted single MEH-PPV fibre, for various collection angles and TE polarization of the guided mode. The 0–0 and 0–1 vibronic replicas of the untextured MEH-PPV fibre, obtained by fitting this spectrum with a Gaussian superposition, are shown as blue curves. The arrows indicate the angular dependence of the emission peaks. c, Angular dispersion of the Bragg-outcoupled modes with s- (that is, for TE guided modes, filled circles) and p- (transverse magnetic (TM), open circles) polarizations. The error bar shown is the same for all points. The lines are guides for the eye. d, Wavelength dependence of the effective refractive index of the Bragg-outcoupled TE (filled circles) and TM (open diamonds) modes of the nanoimprinted fibre, and of the corresponding difference,  $\Delta n_{\text{eff}} = \Delta n_{\text{eff,TE}} - n_{\text{eff,TM}}$  (open circles). The dotted line is a guide for the eye.

### 3.6. Optical sensors

Single-nanowire detection presents special advantages of high sensitivity and fast response and may offer potentials for highly localized sensing with small footprint and high spatial resolution, as have been recently demonstrated in single-polymer-nanowire electrical sensors [88,89]. And optical sensing offers potentials of high sensitivity, fast response, immunity to electromagnetic interference, and safe operation in explosive or combusive atmosphere, as well as more options for signal retrieval from optical intensity, spectrum, phase, polarization, and fluorescence lifetime [90]. L. Tong group have demonstrated that polymer single-nanowire optical sensors with extraordinary fast response and high sensitivity for humidity and gas sensing [37,91].

When blended or doped with other functional materials, polymer nanowires can be used for optical sensing with high versatilities. For instance, here a 250-nm-diameter PANI/PS nanowire was employed for gas sensing. The nanowire is drawn from a polymer-blend solution of 2 wt % PANI doped with 10-camphorsulfonic and 5 wt% PS in chloroform and is suspended by a 250- $\mu\text{m}$ -width  $\text{MgF}_2$  microchannel and optically connected to fiber tapers at both ends. The sensor is operated by applying a nitrogen-diluted  $\text{NO}_2$  gas onto the nanowire with a probing light of 532-nm wavelength. When exposed to  $\text{NO}_2$ , the increase of the oxidation degree of PANI results in spectral absorption at the wavelength of the probing light, in which the absorbance is proportional to the degree of the oxidation that increases with the concentration of  $\text{NO}_2$ . Figure 24a shows a typical response of a 250-nm-diameter PANI/PS nanowire to 1 ppm  $\text{NO}_2$ . A clear absorbance is observed, with a response time of about 7s, which is orders of magnitude faster than in other types of  $\text{NO}_2$  sensors [92]. The time-dependent absorbance of the nanowire at room temperature to cyclic  $\text{NO}_2$ /nitrogen exposure with  $\text{NO}_2$  concentration from 0.1 to 4 ppm is given in Figure 24b, indicating good reversibility of the nanowire response. The linear dependence of the absorbance over the  $\text{NO}_2$  concentration (see inset) suggests that the PANI/PS nanowire could function as a  $\text{NO}_2$  optical sensor with a detection limit below 0.1 ppm.

For optical sensing, we suspended a QD/PS nanofiber across a 245- $\mu\text{m}$ -wide  $\text{MgF}_2$  microchannel with two ends of the NF coupled to fiber tapers for optical launching and signal collection, as schematically illustrated in Figure 25a. For robustness, the coupling region between the QD/PS NF and fiber tapers was bonded to the substrate using low-index UV-cured fluoropolymer (EFIRON PC-373; Luvantix Co. Ltd.), and the sensing element was sealed inside a glass chamber. To operate the sensor for humidity sensing, 532 nm excitation light was launched from the left-hand fiber taper, and measured the light output from the right-hand fiber taper, while changing the surrounding relative humidity (RH) from 7% to 81% by circulating moisture gases inside the chamber. The optical response of the nanofiber sensor is shown in Fig. 25b, which works well with the excitation power of about 100 pW used here. The RH-dependent PL intensity can be attributed to the passivation of surface trap states of QDs by water molecules [93-95]. The monotonic increase of the PL output with increasing RH can be used for RH sensing, with



estimated resolution (calculated from the response curve in Figure 25b) better than 1% RH. Excellent reversibility of the nanofiber sensor was obtained on alternately cycling 19% and 54% RH air, as shown in Figure 25c. The instant response of the sensor was investigated by introducing sudden changes of the humidity in the chamber, with measured response time less than 90 ms (Figure 25d), which is 1–2 orders of magnitude faster than those of RH sensors based on films or monolayers [96–98]. In addition, the PL intensity of the CdSe/ZnS QD-doped PS matrix was also found to be sensitive to other species, such as CN-ions [99]; the nanofiber sensor proposed here is promising for optical detection of many other types of samples.

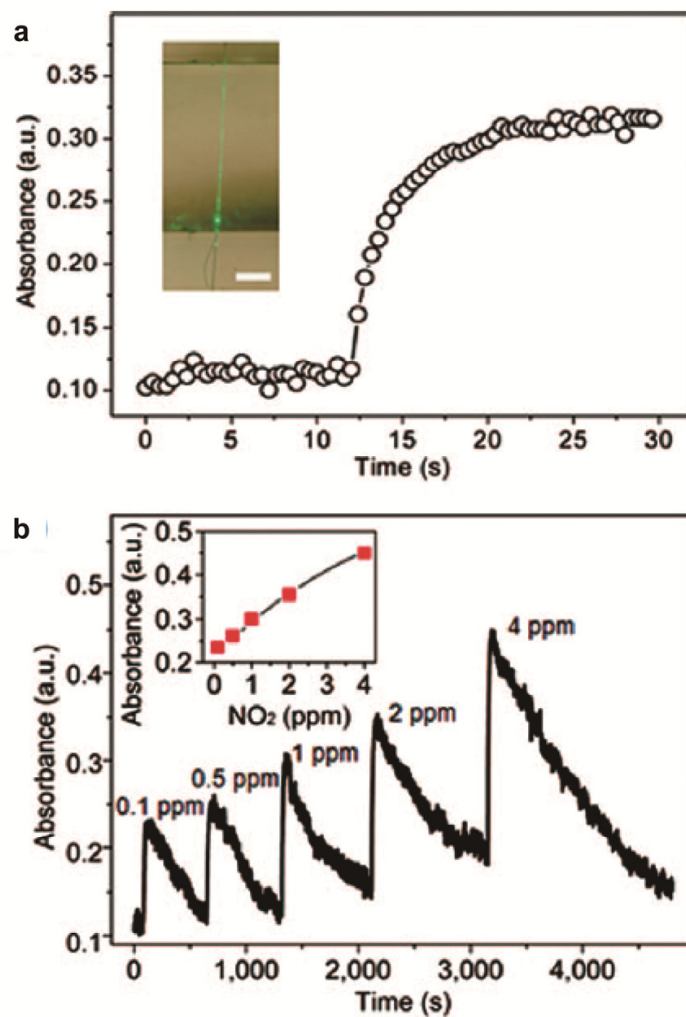


**Figure 24.** PANI/PS single-nanowire  $\text{NO}_2$  sensors [37]. (a) Optical response of a 250-nm-diameter PANI/PS nanowire to 1 ppm  $\text{NO}_2$  with a 532-nm-wavelength light. Inset, a close-up optical micrograph of the sensing element with a 532-nm-wavelength probing light guided along the nanowire. Scale bar, 50  $\mu\text{m}$ . (b) Time dependent absorbance of the nanowire to cyclic  $\text{NO}_2$ /nitrogen exposure with  $\text{NO}_2$  concentration from 0.1 to 4 ppm. Inset, dependence of the absorbance over the  $\text{NO}_2$  concentration ranging from 0.1 to 4 ppm.

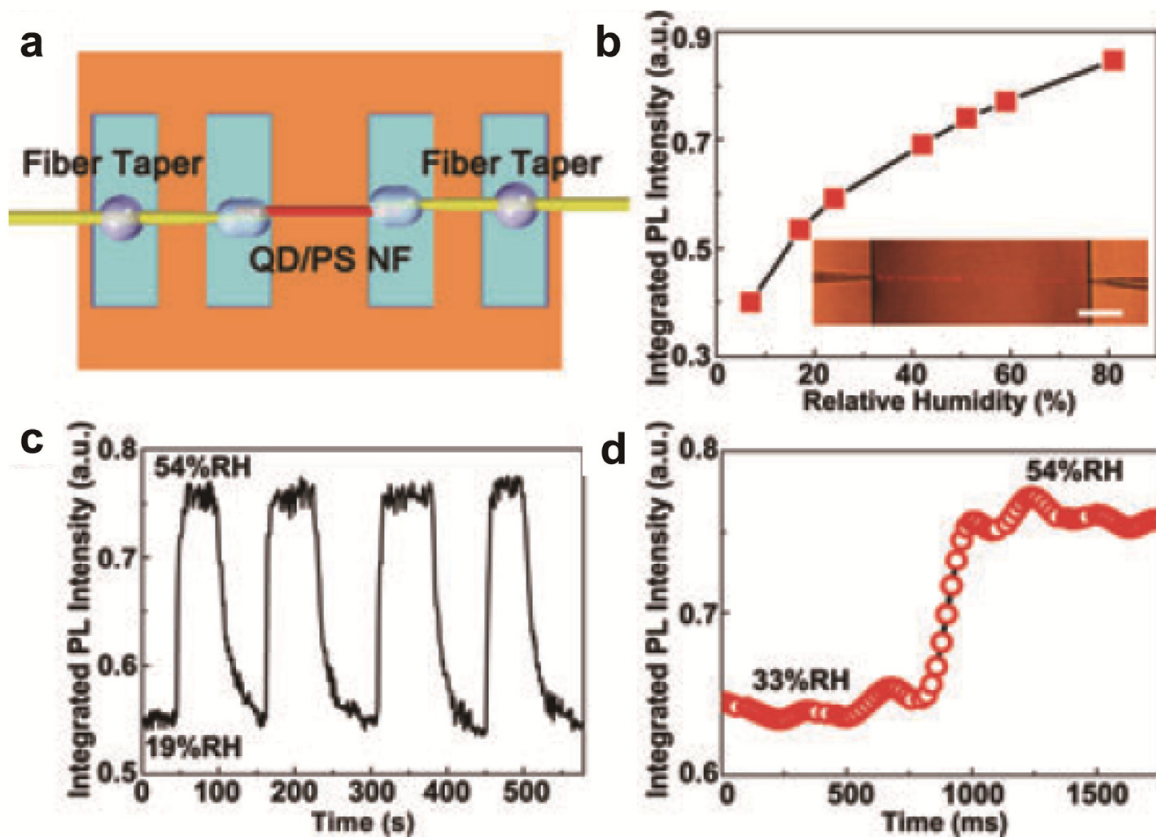


**Figure 25.** QD/PS single-NF humidity sensors [91]. a) Schematic illustration of the sensor. b) Integrated PL intensity of the nanofiber exposed to ambient RH ranging from 7% to 81%. Inset: Optical microscopy image of the waveguided-light-excited 480-nm-diameter 245- $\mu\text{m}$ -long QD/PS nanofiber used in the sensor. Scale bar: 50  $\mu\text{m}$ . c) Response of the nanofiber sensor to alternately cycled 54% and 19% RH air. d) Typical time-dependent integrated PL intensity of the nanofiber reveals a response time of about 90 ms when RH jumps from 33% to 54%.

#### 4. Polymeric nanowire architecture as full-color micro/nanodisplays

Recently, a number of crossed nanofiber structures for full-color micro/nanodisplays has been reported by H. Yu et al. [22] The crossed array structures were formed by assembling flexible PTT nanofibers under an optical microscope with the assistance of micromanipulators while avoiding the use of color filters and complicated photolithography processing. The color pixels of the displays consist of micro/nanometer sized color spots in a radius of 300–1500 nm. The colors and sizes of the spots were tuned by changing the total power and power ratios of the launched red, green, and blue (RGB) lights.

As shown in Fig. 26a, a 3 $\times$ 3 structure was assembled by using nanofibers 1, 2, and 3 with diameters of 558, 598, and 598 nm, respectively, and RGB lights were launched into the nanofibers 1, 2, and 3, respectively, with a total power of 63.4  $\mu\text{W}$  and a power ratio of about 50:13: 10. Inset of Figure 25b shows that a white colour at the centre of the spot with a radius of about 818 nm was observed at the crossed junction. The colour coordinate was (0.41, 0.35). Its correlated colour temperature (CCT) is 3026 K.

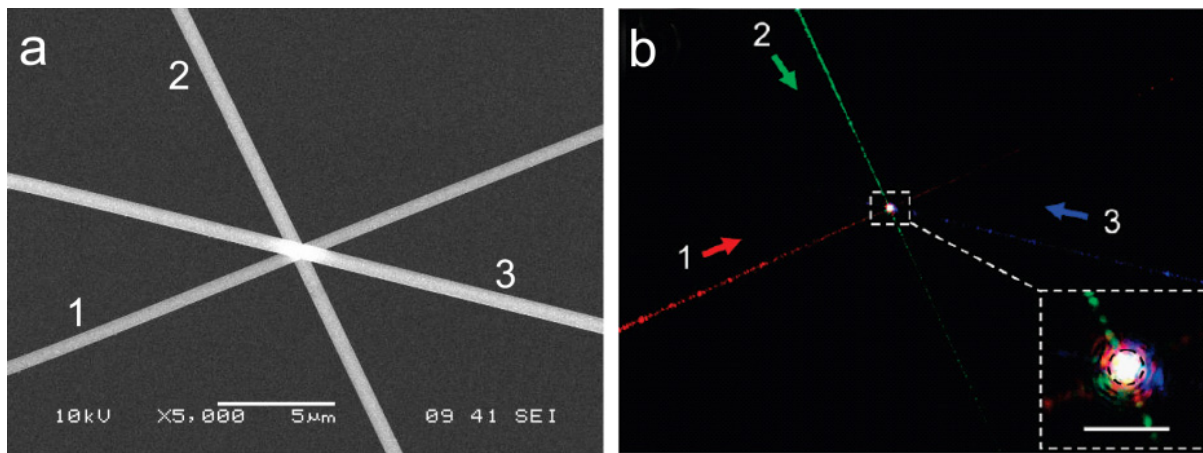


**Figure 26.** 3×3 crossed structure [22]. (a) SEM image of the device with diameter of 558, 598, and 598 nm for the nanofibers 1, 2, and 3, respectively. The nanofiber 1 is perpendicular to the nanofiber 2, the cross-angle of the nanofibers 2 and 3 is about 50°. (b) Optical microscope image of the guided visible lights in the structure. The inset shows a magnified (×5) view of the white spot at the crossed junction. The arrows show the propagation directions of the launched lights. Scale bar in the inset is 20 µm.

## 5. Potential to construct integrated optical circuit

The requirement for any photonic device in optical computing, data communications or telecommunications is to be robust, lowcost, high speed and easy to integrate. Polymer MNFs are an ideal material for assembling structures that address both of these requirements, as they offer lowcost processing and are easy to integrate into existing and future networks made either entirely from polymeric or a combination of polymeric with semiconductive. In addition, polymer MNFs possess many other advantages such as versatility for biofunctionalization, and the promotion of specific desired cell behaviors that are elicited by the nanofibers architecture. Polymer MNF shave can be easily produced by current technique, which exhibiting many advantages such as mechanical flexibility, perm-selective nature to gas molecules, biocompatibility, easy processing, and low cost. It is demonstrated that polymer nanofibers offer a unique materials platform for producing key photonic elements including lasing, light emitting diode, detectors, cavity resonator, and passive elements. All these indicate that polymer MNFs is an promising candidate for integrated optical circuit with high density and multifunction. As an excellent research platform merging fiber-optic technology and nanotechnology, there is no doubt that polymer MNFs will continue to open up new opportunities in broad areas including micro- and nanoscale photonics, nonlinear optics and quantum optics in the near future.

### Author details

Xiaobo Xing

*Education Ministry's Key Laboratory of Laser Life Science & Institute of Laser Life Science, College of Biophotonics, South China Normal University, Guangzhou, Guangdong, China  
Department of Chemistry, Jinan University, Guangdong, Guangzhou, 510632, China*

Huaqing Yu

*School of Physics and Electronic-information Engineering, Hubei Engineering University,  
Xiaogan, China*

Debin Zhu

*Education Ministry's Key Laboratory of Laser Life Science & Institute of Laser Life Science,  
College of Biophotonics, South China Normal University, Guangzhou, Guangdong, China*

Jiapeng Zheng

*School of Physics and Optoelectronic Science and Engineering, South China Normal University,  
Guangzhou, Guangdong, China*

Huang Chen

*School of Information and Optoelectronic Science and Engineering, South China Normal University,  
Guangzhou, Guangdong, China*

Wei Chen

*School of Information and Optoelectronic Science and Engineering, South China Normal University,  
Guangzhou, Guangdong, China*

Ruibin Xie

*School of Information and Optoelectronic Science and Engineering, South China Normal University,  
Guangzhou, Guangdong, China*

Jiye Cai

*Department of Chemistry, Jinan University, Guangdong, Guangzhou, 510632, China*

## 6. Acknowledgement

The work thanks for Prof. Baojun Li from State Key Laboratory of Optoelectronic Materials and Technologies, School of Physics and Engineering, Sun Yat-Sen University, for his guidance. This work was supported by China's National Natural Science Foundation (6117707, 81071790, 11104162), China Postdoctoral Science Foundation Funded Project (201003359), Guangdong Excelent Doctoral Dissertation Funded Project (SYBZZM201126), the Key Project of Chinese Ministry of Education (211131), the Science and Technology Project of Guangzhou Nansha District (RG201001003).

## 7. References

- [1] D. Appell. Wired for success. *Nature*, 419, 553-555 (2002).
- [2] M. Law, D. J. Sirbuly, J. C. Johnson, J. Goldberger, R. J. Saykally, and P. Yang. Nanoribbon waveguides for subwavelength photonics integration. *Science*, 305, 1269-1273 (2004).
- [3] Y. Xia, P. Yang, Y. Sun, Y. Wu, B. Mayers, B. Gates, Y. Yin, F. Kim, and Y. Yan. One-dimensional nanostructures: synthesis, characterization, and applications. *Adv. Mater.*, 15, 353-389 (2003).
- [4] Y. Huang, X. Duan, Y. Cui, L. Lauhon, K.-H. Kim, and C. Lieber. Logic gates and computation from assembled nanowire building blocks. *Science*, 294, 1313-1317 (2001).



- [5] J. Wang, M. Gudiksen, X. Duan, Y. Cui, and C. Lieber. Highly polarized photoluminescence and photodetection from single indium phosphide nanowires. *Science*, 293, 1455-1457 (2001).
- [6] H. Kind, H. Yan, B. Messer, M. Law, and P. Yang. Nanowire ultraviolet photodetectors and optical switches. *Adv. Mater.*, 14, 158-160 (2002).
- [7] M. Law, H. Kind, B. Messer, F. Kim, P. Yang. Photochemical sensing of NO<sub>2</sub> with SnO<sub>2</sub> nanoribbon nanosensors at room temperature. *Angew. Chem. Int. Ed.*, 41, 2405-2408 (2002).
- [8] J. P. Zhang, D. Y. Chu, S. L. Wu, S. T. Ho, W. G. Bi, C.W. Tu, and R. C. Tiberio. Photonic-wire laser. *Phys. Rev. Lett.*, 75, 2678-2681 (1995).
- [9] X. Duan, Y. Huang, R. Agarwal, and C. M. Lieber. Single-nanowire electrically driven lasers. *Nature*, 421, 241-245 (2003).
- [10] L. Tong, R. R. Gattass, J. B. Ashcom, S. He, J. Lou, M. Shen, I. Maxwell, and E. Mazur. Subwavelength-diameter silica wires for low-loss optical wave guiding. *Nature*, 426, 816-819 (2003).
- [11] A. L. Pyayt, B. Wiley, Y. Xia, A. T. Chen and L. Dalton. Integration of photonic and silver nanowire plasmonic waveguides. *Nat. Nanotechnol.*, 3, 660-665 (2008).
- [12] G. Brambilla, F. Xu, and X. Feng. Fabrication of optical fiber nanowires and their optical and mechanical characterization. *Electron. Lett.*, 42, 517-518 (2006).
- [13] L. Tong, J. Lou, R. R. Gattass, S. He, X. Chen, L. Liu, and E. Mazur. Assembly of silicananowires on silica aerogels for microphotonic devices. *Nano. Lett.*, 5, 259-262(2005).
- [14] Y. Li and L. Tong. Mach-Zehnder interferometers assembled with optical microfibers or nanofibers. *Opt. Lett.*, 33, 303-305 (2008).
- [15] S. A. Harfenist, S. D. Cambron, E. W. Nelson, S. M. Berry, A. W. Isham, M. M. Crain, K. M. Walsh, R. S. Keynton, and R. W. Cohn. Direct drawing of suspended filamentary micro- and nanostructures from liquid polymers. *Nano. Lett.*, 4, 1931-1937 (2004).
- [16] H. Liu, J. B. Edel, L. M. Bellan, and H. G. Craighead. Electrospun polymer nanofibers as subwavelength optical waveguides incorporating quantum dots. *Small*, 2, 495-499 (2006).
- [17] X. B. Xing, Y. Q. Wang, H. Zhu, and B. J. Li. Nanofiber drawing and nanodevice assembly in poly(trimethylene terephthalate). *Opt. Express*, 16, 10815-10822 (2008).
- [18] X. B. Xing, H. Zhu, Y. Q. Wang, and B. J. Li. Ultra Compact photonic coupling splitters twisted by PTT nanowires. *Nano.Lett.*, 8, 2839-2843 (2008).
- [19] H. Zhu, Y. Q. Wang, and B. J. Li. Tunable refractive index sensor with ultracompact structure twisted by poly(trimethylene terephthalate) nanowires. *ACS Nano*, 3, 3110-3114 (2009).
- [20] M. L. Guo, J. C. Shi, and B. J. Li. Polymer-based micro/nanowire structures for three-dimensional photonic integration. *Opt. Lett.*, 33, 2104-2106 (2008).
- [21] Y. Q. Wang, H. Zhu, and B. J. Li. Cascaded Mach-Zehnder interferometers assembled by submicron PTT wires. *Photon. Technol. Lett.*, 21, 1115-1117(2009).
- [22] H. Yu, D. Liao, M. B. Johnston, and B. Li. All-optical full-color displays using polymer nanofibers. *ACS Nano*, 5, 2020-2025 (2011).
- [23] J. A. Merlo, C. D. Frisbie. Field effect conductance of conducting polymer nanofibers. *J. Polym. Sci. Part B: Polym. Phys.*, 41, 2674-2680 (2003).

- [24] J. A. Merlo, C. D. Frisbie. Field effect transport and trapping in regioregular polythiophene nanofibers. *J. Phys. Chem. B*, 108, 19169-19179 (2004).
- [25] H. Liu, C. H. Reccius, and H. G. Craighead. Single electrospun regioregular poly(3-hexylthiophene) nanofiber field-effect transistor. *Appl. Phys. Lett.*, 87, 253106 (2005).
- [26] C. R. L. P. N. Jeukens, P. Jonkheijm, F. J. P. Wijnen, J. C. Gielen, P. C. M. Christianen, A. P. H. Schenning, E. W. Meijer, and J. C. Maan. Polarized emission of individual self-assembled oligo(p-phenylenevinylene)-based nanofibers on a solid support. *J. Am. Chem. Soc.*, 127, 8280-8281 (2005).
- [27] K. Kim, J. Jin. Preparation of PPV nanotubes and nanorods and carbonized products derived therefrom. *Nano Lett.*, 1, 631-636 (2001).
- [28] M. Steinhart, J. H. Wendorff, A. Greiner, R. B. Wehrspohn, K. Nielsch, J. Schilling, J. Choi, and U. Gosele. Polymer nanotubes by wetting of ordered porous templates. *Science*, 296, 1997 (2002).
- [29] V. Beachley, X. Wen. Polymer nanofibrous structures: Fabrication, biofunctionalization, and cell interaction. *Prog. Polym. Sci.*, 35, 868-892 (2010).
- [30] X. Xing, H. Zhu, Y. Wang, and B. Li. Ultrasmall optical beam splitters assembled by polymer nanowires. *Phys. Express*, 1, 89-92 (2011).
- [31] Y. Wang, H. Zhu, B. Li. Optical characterization of mechanically tunable microwire based resonators by changing ring radius and wire diameter. *Opt. Commun.*, 284, 3276-3279 (2011).
- [32] J. Shi, M. Guo, and B. Li. Assembly of arbitrary and vertical optical couplers using flexible polymer micro/nanowires. *Appl. Phys. Lett.*, 93, 121101 (2008).
- [33] Y. Wang, H. Zhu, and B. Li. Cascaded Mach-Zehnder interferometers assembled by submicrometer PTT wires. *IEEE. Photon. Technol. Lett.*, 21, 1115-1117 (2009).
- [34] F. Gu, H. Yu, P. Wang, Z. Yang, and L. Tong. Light-emitting polymer single nanofibers via waveguiding excitation. *ACS Nano*, 4, 5332-5338 (2010).
- [35] G. A. O'Brien, A. J. Quinn, D. A. Tanner, and G. Redmond. A single polymer nanowire photodetector. *Adv. Mater.*, 18, 2379-2383 (2006).
- [36] F. Quochi, F. Cordella, A. Mura, G. Bongiovanni, F. Balzer, and H.-G. Rubahn. One-dimensional random lasing in a single organic nanofiber. *J. Phys. Chem. B*, 109, 21690-21693 (2005).
- [37] F. Gu, L. Zhang, X. Yin, and L. Tong. Polymer single-nanowire optical sensors. *Nano Lett.*, 8, 2757-2761 (2008).
- [38] J. Kameoka, D. Czaplewski, H. Liu, and H. G. Craighead. Polymeric nanowire architecture. *J. Mater. Chem.*, 14, 1503-1505 (2004).
- [39] R. Vasita, D. S. Katti. Nanofibers and their applications in tissue engineering. *Int. J. Nanomed.*, 1, 15-30 (2006).
- [40] V. Beachley, X. Wen. Fabrication of nanofiber reinforced protein structures for tissue engineering. *Mater. Sci. Eng. C Biol. Appl.*, 29, 2448-2453 (2009).
- [41] P. X. Ma, R. Zhang. Synthetic nano-scale fibrous extracellular matrix. *J. Biomed. Mater. Res.*, 46, 60-72 (1999).
- [42] S. Ramakrishna, K. Fujihara, W. E. Teo, T. C. Lim, and Z. Ma. An introduction to electrospinning and nanofibers. Singapore: World Scientific Publishing Company, 2005, 396pp.

- [43] P. Berndt, G. Fields, and M. Tirrell. Synthetic lipidation of peptides and amino acids: monolayer structure and properties. *J. Am. Chem. Soc.*, 117, 9515-9522 (1995).
- [44] H. Jun, V. Yuwono, S. Paramonov, and J. Hartgerink. Enzyme mediated degradation of peptide-amphiphile nanofiber network. *Adv. Mater.*, 17, 2612-2617 (2005).
- [45] J. D. Hartgerink, E. Beniash, and S. I. Stupp. Self-assembly and mineralization of peptide-amphiphile nanofibers. *Science*, 294, 1684-1688 (2001).
- [46] G. A. Silva, C. Czeisler, K.L. Niece, E. Beniash, D. A. Harrington, J. A. Kessler, and S. I. Stupp. Selective differentiation of neural progenitor cells by high-epitope density nanofibers. *Science*, 303, 1352-1355 (2004).
- [47] H. Yokoi, T. Kinoshita, and S. Zhang. Dynamic reassembly of peptide RADA16 nanofiber scaffold. *Proc. Natl. Acad. Sci., USA*, 102, 8414-8419 (2005).
- [48] H. Jeong, S. Lee, P. Kim, and K. Suh. Stretched polymer nanohairs by nanodrawing. *Nano Lett.*, 6, 1508-1513 (2006).
- [49] S. Grimm, R. Giesa, K. Sklarek, A. Langner, U. Gosele, H. W. Schmidt, and M. Steinhart. Nondestructive replication of self-ordered nanoporous alumina membranes via cross-linked polyacrylate nanofiber arrays. *Nano Lett.*, 8, 1954-1959 (2008).
- [50] J. R. Porter, A. Henson, and K. C. Popat. Biodegradable poly(epsilon-caprolactone) nanowires for bone tissue engineering applications. *Biomaterials*, 30, 780-788 (2009).
- [51] S. L. Tao, T. A. Desai. Aligned arrays of biodegradable poly(epsilon-caprolactone) nanowires and nanofibers by template synthesis. *Nano Lett.*, 7, 1463-1468 (2007).
- [52] D. A. Rollings, S. Tsoi, J. C. Sit, and J. G.C. Veinot. Formation and aqueous surface wettability of polysiloxane nanofibers prepared via surface initiated, vapor-phase polymerization of organotrichlorosilanes. *Langmuir*, 23, 5275-5278 (2007).
- [53] P. Mankidy, R. Rajagopalan, and H. Foley. Facile catalytic growth of cyanoacrylate nanofibers. *Chem. Commun.*, 1139-1141 (2006).
- [54] A. Alemdar, M. Sain. Isolation and characterization of nanofibers from agricultural residues: wheat straw and soy hulls. *Bioresour. Technol.*, 99, 1664-1671 (2008).
- [55] T. H. Fischer, C. R. Valeri, C. J. Smith, C. M. Scull, E. P. Merricks, T. C. Nichols, M. Demcheva, and J. N. Vournakis. Non-classical processes in surface hemostasis: mechanisms for the poly-N-acetyl glucosamine-induced alteration of red blood cell morphology and surface prothrombogenicity. *Biomed. Mater.*, 3, 015009/1-9 (2008).
- [56] Y. Fan, T. Saito, A. Isogai. Preparation of chitin nanofibers from squid pen  $\beta$ -chitin by simple mechanical treatment under acid conditions. *Biomacromolecules*, 9, 1919-1923 (2008).
- [57] Aden Brook Farms Website. Large 3x3 bales of brightwheat straw; 2009 [http://adenbrookfarms.com/order/index.php?main\\_page=index&cPath=2](http://adenbrookfarms.com/order/index.php?main_page=index&cPath=2).
- [58] X. Jing, Y. Wang, D. Wu, J. Qiang. Sonochemical synthesis of polyaniline nanofibers. *Ultrason. Sonochem.*, 14, 75-80 (2007).
- [59] D. Li, J. Huang, R. B. Kaner. Polyaniline nanofibers: a unique polymer nanostructure for versatile applications. *Acc. Chem. Res.*, 42, 135-145 (2009).
- [60] W. K. Czaja, D. J. Young, M. Kawecki, and J. R. M. Brown. The future prospects of microbial cellulose in biomedical applications. *Biomacromolecules*, 8, 1-12 (2007).
- [61] J. Jang, M. Chang, and H. Yoon. Chemical sensors based on highly conductive Poly(3,4-ethylene-dioxythiophene) nanorods. *Adv. Mater.*, 17, 1616-1620 (2005).

- [62] H. Kong, J. Jang. One-step fabrication of silver nanoparticle embedded polymer nanofibers by radical-mediated dispersion polymerization. *Chem. Commun.*, 3010-3012 (2006).
- [63] P. P. Bishnu. *Fundamentals of fibre optics in telecommunication and sensor systems*. John Wiley & Sons, New York, 1992.
- [64] D. K. Mynbaev, and L. L. Scheiner. *Fiber-optic communications technology*. PrenticeHall, New York, 2001.
- [65] A. Mendez, T. F. Morse. *Specialty optical fibers handbook*. Academic Press, Burlington, 2007.
- [66] T. Kawazoe, T. Yatsui, and M. Ohtsu. Nanophotonics using optical near fields. *J. Non-Cryst. Solids*, 352, 2492-2495 (2006).
- [67] L. Tong, M. Sumetsky. *Subwavelength and nanometer diameter optical fibers*. Springer, Zhejiang University Press, 2009.
- [68] R. Yan, D. Gargas, and P. Yang. Nanowire photonics. *Nat. Photon*, 3, 569-576 (2009).
- [69] Y. Hung, X. Duan, and C. M. Lieber. Nanowires for integrated multicolor nanophotonics. *Small*, 1, 142-147 (2005).
- [70] D. K. Mynbaev, and L. L. Scheiner. *Fiber-optic communications technology*. Prentice Hall: Upper Saddle River, N.J., 2002.
- [71] P. Urquhart. Review of rare earth doped fiber lasers and amplifiers. *Proc. IEE, Part J*, 135, 385-407 (1988).
- [72] H. Ma, A. K.-Y. Jen, L. R. Dalton. Polymer-based optical waveguides: materials, processing, and devices. *Adv. Mater.*, 14, 1339-1365 (2002).
- [73] H. Yu, R. Zhang, and B. Li. Optical properties of quantum-dot-decorated polymer nanofibers. *Nanotechnology*, 22, 335202 (2011).
- [74] Q. Song, L. Liu, and L. Xu. Lasing action in dye doped polymer nanofiber knot resonator. *J. Lightwave Technol.*, 27, 4374-4376 (2009).
- [75] H. Sirringhaus, N. Tessler, and R. H. Friend. Integrated optoelectronic devices based on conjugated polymers. *Science*, 280, 1741-1744 (1998).
- [76] F. Carpi, D. De Rossi. Colours from electroactive polymers: electrochromic, electroluminescent and laser devices based on organic materials. *Opt. Laser Technol.*, 38, 292-305 (2006).
- [77] N. Tessler, G. J. Denton, and R. H. Friend. Lasing from conjugated-polymer microcavities. *Nature*, 382, 695-697 (1996).
- [78] S. V. Frolov, M. Shkunov, Z. V. Vardeny, and K. Yoshino. Ring microlasers from conducting polymers. *Phys. Rev. B*, 56, R4363-R4366 (1997).
- [79] G. Heliotis, R. Xia, G. A. Turnbull, P. Andrew, W. L. Barnes, I. D. W. Samuel, and D. C. Bradley. Emission characteristics and performance comparison of polyfluorene lasers with one- and two-dimensional distributed feedback. *Adv. Funct. Mater.*, 14, 91-97 (2004).
- [80] S. Riechel, C. Kallinger, U. Lemmer, J. Feldmann, A. Gombert, V. Wittwer, and U. Scherf. A nearly diffraction limited surface emitting conjugated polymer laser utilizing a two-dimensional photonic band structure. *Appl. Phys. Lett.*, 77, 2310-2312 (2000).
- [81] D. O'carroll, I. Liberwirth, and G. Redmond. Microcavity effects and optically pumped lasing in single conjugated polymer nanowires. *Nat. Nanotechnol.*, 2, 180-184 (2007).
- [82] R. Xia, G. Heliotis, Y. Hou, and D. D. C. Bradley. Fluorene-based conjugated polymer optical gain media. *Org. Electron.*, 4, 165-177 (2003).



- [83] M. Ariu, D. G. Lidzey, M. Sims, A. J. Cadby, P. A. Lane, and D. D. C. Bradley. The effect of morphology on the temperature-dependent photoluminescence quantum efficiency of the conjugated polymer poly(9,9-dioctylfluorene). *J. Phys.: Condens. Matter.*, 14, 9975-9986 (2002).
- [84] S. R. Forrest. The path to ubiquitous and low-cost organic electronic appliances on plastic. *Nature*, 428, 911-918 (2004).
- [85] G. Malliaras, R. Friend. An organic electronics primer. *Phys. Today*, 58, 53-58 (2005).
- [86] E. Menard, M. A. Meitl, Y. Sun, J.-U. Park, D. J.-L. Shir, Y.-S. Nam, S. Jeon, and J. A. Rogers. Micro and nanopatterning techniques for organic electronic and optoelectronic systems. *Chem. Rev.*, 107, 1117-1160 (2007).
- [87] F. D. Benedetto, A. Camposeo, S. Pagliara, E. Mele, L. Persano, R. Stabile, R. Cingolani, and D. Pisignano. Patterning of light-emitting conjugated polymer nanofibres. *Nat. Nanotechnol.*, 3, 614-619, (2008).
- [88] H. Q. Liu, J. Kameoka, D. A. Czaplewski, and H. G. Craighead. Polymeric nanowire chemical sensor. *Nano Lett.*, 4, 671-675 (2004).
- [89] K. Ramanathan, M. A. Bangar, M. Yun, W. Chen, N. V. Myung, and A. Mulchandani. Bioaffinity sensing using biologically functionalized conducting-polymer nanowire. *J. Am. Chem. Soc.*, 127, 496-497 (2005).
- [90] William B. Spillman Jr. Fiber optical sensors. An introduction for engineers and scientists. John Wiley & Sons, Inc., Hoboken, New Jersey, 2001.
- [91] C. Meng, Y. Xiao, P. Wang, L. Zhang, Y. Liu, and L. Tong. Quantum-dot-doped polymer nanofibers for optical sensing. *Adv. Mater.*, 23, 1514-1544 (2011).
- [92] M. C. McAlpine, H. Ahmad, D. W. Wang, and J. R. Heath. Highly ordered nanowire arrays on plastic substrates for ultrasensitive flexible chemical sensors. *Nat. Mater.*, 6, 379-384 (2007).
- [93] S. R. Cordero, P. J. Carson, R. A. Estabrook, G. F. Strouse, and S. K. Buratto. Photoactivated luminescence of CdSe quantum dot monolayers. *J. Phys. Chem. B*, 104, 12137-12142 (2000).
- [94] B. Alpers, I. Rubinstein, and G. Hodes. Identification of surface states on individual CdSe quantum dots by room-temperature conductance spectroscopy. *Phys. Rev. B*, 63, 081303 (2001).
- [95] M. Jones, J. Nedeljkovic, R. J. Ellingson, A. J. Nozik, and G. Rumbles. Photoenhancement of luminescence in colloidal CdSe quantum dot solutions. *J. Phys. Chem. B*, 107, 11346-11352 (2003).
- [96] S. K. Khijwania, K. L. Srinivasan, and J. P. Singh. An evanescent-wave optical fiber relative humidity sensor with enhanced sensitivity. *Sens. Actuators, B*, 104, 217-222 (2005).
- [97] Y. Zhang, K. Yu, D. Jiang, Z. Zhu, H. Geng, and L. Luo. Zinc oxide nanorod and nanowire for humidity sensor. *Appl. Surf. Sci.*, 242, 212-217 (2005).
- [98] R. A. Barry, P. Wiltzius. Humidity-sensing inverse opal hydrogels. *Langmuir*, 22, 1369-1374 (2006).
- [99] A. Touceda-Varela, E. I. Stevenson, J. A. Galve-Gasion, D. T. F. Dryden, J. C. Mareque-Rivas. Selective turn-on fluorescence detection of cyanide in water using hydrophobic CdSe quantum dots. *Chem. Commun.*, 1998-2000 (2008).